Wear 358-359 (2016) 32–50

Contents lists available at ScienceDirect

Wear

journal homepage: www.elsevier.com/locate/wear

Sliding and abrasive wear behaviour of HVOF- and HVAF-sprayed Cr_3C_2–NiCr hardmetal coatings

G. Bolelli [a,*], L.-M. Berger [b,1], T. Börner [a,b,2], H. Koivuluoto [c], V. Matikainen [c], L. Lusvarghi [a], C. Lyphout [d], N. Markocsan [d], P. Nylén [d], P. Sassatelli [a], R. Trache [b], P. Vuoristo [c]

[a] Dipartimento di Ingegneria "Enzo Ferrari", University of Modena and Reggio Emilia, Via P. Vivarelli 10/1, I-41125 Modena, MO, Italy
[b] Fraunhofer-Institut für Werkstoff- und Strahltechnik (IWS), Winterbergstr. 28, D-01277 Dresden, Germany
[c] Department of Materials Science, Tampere University of Technology, Korkeakoulunkatu 6, FI-33720 Tampere, Finland
[d] Department of Engineering Science, University West, Gustava Melins gata 2, SE-461 86 Trollhättan, Sweden

ARTICLE INFO

Article history:
Received 24 December 2015
Received in revised form
29 March 2016
Accepted 30 March 2016
Available online 6 April 2016

Keywords:
Thermal spray coatings
Cermets
Three-body abrasion
Sliding wear
High temperature
Indentation

ABSTRACT

This paper provides a comprehensive characterisation of HVOF- and HVAF-sprayed Cr_3C_2–25 wt.% NiCr hardmetal coatings. One commercial powder composition with two different particle size distributions was processed using five HVOF and HVAF thermal spray systems.

All coatings contain less Cr_3C_2 than the feedstock powder, possibly due to the rebound of some Cr_3C_2-rich particles during high-velocity impact onto the substrate.

Dry sand-rubber wheel abrasive wear testing causes both grooving and pull-out of splat fragments. Mass losses depend on inter- and intra-lamellar cohesion, being higher ($\geq$ 70 mg after a wear distance of 5904 m) for the coatings deposited with the coarser feedstock powder or with one type of HVAF torch.

Sliding wear at room temperature against alumina involves shallower abrasive grooving, small-scale delamination and carbide pull-outs, and it is controlled by intra-lamellar cohesion. The coatings obtained from the fine feedstock powder exhibit the lowest wear rates ($\approx 5\text{x}10^{-6}$ mm^3/(Nm)). At 400 °C, abrasive grooving dominates the sliding wear behaviour; wear rates increase by one order of magnitude but friction coefficients decrease from $\approx$0.7 to $\approx$0.5. The thermal expansion coefficient of the coatings ($11.08\text{x}10^{-6}$ °C^{-1} in the 30–400 °C range) is sufficiently close to that of the steel substrate ($14.23\text{x}10^{-6}$ °C^{-1}) to avoid macro-cracking.

1. Introduction

This paper is part of a wider research project aiming to provide a systematic assessment of the properties of hardmetal coatings as a function of the thermal spray deposition process and of the particle size of the feedstock powder. Due to the emergence of a new generation of high velocity air-fuel (HVAF) spray processes [1,2], it is necessary to compare the coating performance with the current state-of-the-art high velocity oxygen-fuel (HVOF) spray processes used in the industrial environment for coating preparation. Following a previous work dealing with the tribology of HVOF– and HVAF–sprayed WC – 10 wt.% Co – 4 wt.% Cr coatings [3], the present one focuses on the sliding and abrasive wear resistance of coatings sprayed with the same processes from a 75 wt.% Cr_3C_2–25 wt.% NiCr feedstock powder with adapted particle size. The technological relevance of this composition is primarily related to its industrial use in tribo-corrosive environments [4] and/or at high temperatures [5–7]. At room temperature, inside the group of hardmetal coatings, HVOF-sprayed Cr_3C_2–NiCr coatings show in most cases the lowest wear resistance for dry and wet abrasive, erosive and sliding wear [8], but, different from WC-based compositions, chromium carbide-based coatings are able to operate up to 800–900 °C due to the low oxidation rate. When operating in atmospheric conditions, due to the protective action of the oxide scale, significant microstructural changes in the coating are observed [9,10]. In addition, the coefficient of thermal expansion ($\approx 10\text{–}11\text{x}10^{-6}$ °C^{-1} [11,12]) of Cr_3C_2–NiCr hardmetal coatings is higher than that of WC-based hardmetals ($\approx 6.9\text{x}10^{-6}$ °C^{-1} [13]) and matches better that of steel substrates, which is a significant additional advantage for high-temperature applications.

Older studies compared plasma-, detonation gun- and HVOF-sprayed Cr_3C_2–NiCr coatings [14–17] and showed the advantages

* Corresponding author.
E-mail address: giovanni.bolelli@unimore.it (G. Bolelli).
[1] Present address: Fraunhofer-Institut für Keramische Technologien und Systeme (IKTS), Winterbergstr. 28, D-01277 Dresden, Germany
[2] Present address: Institut für Korrosionsschutz Dresden GmbH, Gostritzer Str. 65, D-01217 Dresden, Germany

http://dx.doi.org/10.1016/j.wear.2016.03.034
0043-1648/

of high kinetic energy processes (such as HVOF) in terms of density, cohesive strength and tribological properties.

A comparison between the behaviour of Cr_3C_2–NiCr coatings sprayed by HVOF- and HVAF-processes of older generation under particle erosion conditions at high temperatures (up to 900 °C) was provided in a number of papers [6,7,18–22]. These studies underlined how the material response at these temperatures is modified by interlamellar sintering and by the precipitation of a network of secondary chromium carbides within the Ni-based matrix, which provides a strong carbide skeleton network.

The room temperature sliding wear behaviour of HVOF-sprayed Cr_3C_2–NiCr has been investigated in some detail [23–28], but papers dealing with high temperature studies are less abundant. In [29], rotating pin-on-disk tests were performed at 800 °C against an Al_2O_3 ball. At such high temperature, the wear rate was even lower than at room temperature, which was ascribed by the authors to extensive re-precipitation of carbides from the matrix, consistent with the findings from high-temperature erosion tests [18,19]. Similarly, some of the present authors found that, at 700 °C, the wear rate of Cr_3C_2–NiCr coatings against Al_2O_3 in ball-on-disk tests is slightly lower than at room temperature [30]. The authors proposed that the main influencing factor on the results was the formation of an oxide tribofilm on the coating surface. Oxide-based tribofilms were also reported to influence the high-temperature wear behaviour of Cr_3C_2–NiCr coated cylindrical pins sliding against a rotating 100Cr6 steel disk [31]. The tribofilms became increasingly stable and resistant against delamination as the test temperature was raised up to 800 °C, resulting in steadily low friction coefficients. In other works, the sliding wear behaviour of Cr_3C_2–NiCr coatings has been studied, together with that of other hardmetal coatings, at various sliding speeds from 0.1 up to 1 m/s or 3 m/s, and from room temperature up to 600 °C and 800 °C in self-mated pairs and against sintered alumina, respectively [32–34]. In general, at room temperature and 400 °C, both the total wear rates and the coefficients of friction of Cr_3C_2–NiCr coatings depended on the sliding speed. However, in the majority of test conditions, total wear rates were found to be higher, often $> 10^{-5}$ mm³/(Nm), compared to other hardmetal coatings, and coefficients of friction were in an intermediate range (often around 0.6). Details of the wear mechanisms have however not been clarified in those works [32–34], so that further research on the topic is needed. Moreover, in spite of the existence of some comparisons between Cr_3C_2–NiCr coatings obtained by the latest generation of HVOF and HVAF processes under erosion, abrasion and sliding wear conditions [9], a detailed examination of the sliding wear behaviour of HVOF- and HVAF-sprayed Cr_3C_2–NiCr coatings is not yet available. Although the characteristics of the feedstock powder are known to affect the properties of the thermally sprayed Cr_3C_2–NiCr coatings [29,35,36], the corresponding studies are not abundant, apart from some recent work by some of the authors on erosive and abrasive wear [8,9,37,38].

The present research therefore provides a comprehensive assessment of the tribological properties of a range of Cr_3C_2–25 wt.%(Ni-20Cr) hardmetal coatings representative of the state-of-the-art and aims to deepen the relation between the characteristics of the feedstock powder and the sliding and abrasive wear behaviour of the resulting coatings. The coatings were obtained by spraying different feedstock powders using various HVOF and HVAF torches. Tribological testing included dry particle abrasion and sliding wear at room temperature and at 400 °C, a temperature which is pertinent to important industrial application fields such as ball valves for the oil and gas industry, as shown e.g. by manufacturers' catalogues [39,40].

2. Experimental

2.1. Sample manufacturing

One commercial powder composition (Cr_3C_2–25 wt.% Ni-20Cr) with two different particle size distributions (a finer one, hereafter labelled F, and a coarse one, hereafter C), suitable for the HVOF and HVAF spray processes, was provided by one manufacturer and sprayed using five different thermal spray techniques. These include three HVOF torches (two paraffin-fuelled ones and a gas-fuelled one) and two HVAF torches, as summarised in Table 1. For each process, both fractions of powder were sprayed with identical parameter sets. Not all powder-process combinations resulted in satisfactory coating build-up owing to clogging issues into the de Laval nozzle, so that eight distinct coatings were obtained.

Analogously to the previous work on WC–CoCr coatings [3], the substrates were 100 × 50 × 8 mm plates of low-carbon Domex 355 steel (chemical composition, in weight %: C < 0.10, Mn = 1.50, P < 0.025, S < 0.010, Fe = balance), grit-blasted before deposition. The samples were mounted on a rotating turntable and coated using process parameters that were previously optimised for maximum deposition efficiency and coating density. Coating thickness was 300–400 μm in all cases.

2.2. Microstructural and mechanical characterisation of feedstock powders and coatings

The cross-sections of the feedstock powders and of the respective coatings, cold-mounted in epoxy resin, ground and polished with diamond papers, diamond slurries and colloidal silica suspension, were observed by scanning electron microscopy (SEM: XL30 and Quanta-200, FEI, Eindhoven, NL) equipped with energy-dispersive X-ray (EDX) microanalysis (DX-4 EDAX, USA and Inca, Oxford Instruments Analytical, Abingdon, UK). Additional high-magnification micrographs, acquired with a field emission gun-SEM (FEG-SEM: Nova NanoSEM 450, FEI), were employed in order to assess the volume fractions of pores and of carbides by

Table 1
List of powders, deposition techniques and resulting coatings used in this study, together with their conventional designations.

Powder material			Deposition process (designation)				
Composition (wt.%)	**Commercial designation**	**Size (μm) / designation**	**HVAF M3[a]**	**HVOF JP5000[b]**	**HVOF DJ2700[c]**	**HVAF M2[d]**	**HVOF K2[e]**
Cr_3C_2–NiCr 75-25	AMPERIT[f] 584.072	−38 + 10 **F**	M3-F	JP-F	DJ-F	M2-F	/
	AMPERIT [f] 588.074	−45 + 15 **C**	M3-C	JP-C	DJ-C	/	K2-C

[a] M3, Uniquecoat, Oilville, Virginia, USA – fuel: propane.
[b] JP5000, Praxair-Tafa, Concord, NH, USA – fuel: paraffin.
[c] Diamond Jet 2700, Oerlikon-Metco, Wohlen, Switzerland – fuel: propane.
[d] M2, Uniquecoat, Oilville, Virginia, USA – fuel: methane.
[e] K2, GTV Verschleißschutz GmbH, Luckenbach, Germany – fuel: paraffin.
[f] H.C. Starck GmbH, Laufenburg, Germany.

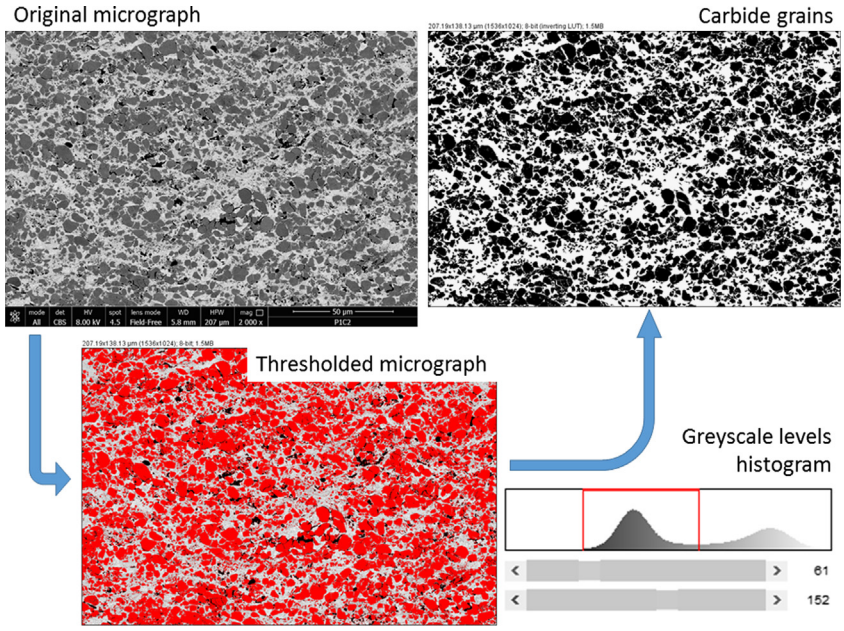

Fig. 1. Example of image thresholding procedure for the identification of carbide grains: thresholding of the original micrograph with isolation of the carbide grains based on their distinctive peak in the greyscale levels histogram.

image analysis, using an image thresholding procedure with the ImageJ software (NIH, Bethesda, Maryland, USA). The analysis was performed on 10 backscattered-electrons SEM micrographs (x2000 magnification) per sample, each having a resolution of 1536×1103 pixels and covering a horizontal field width of 207 µm. The thresholding procedure was based on the greyscale levels histogram, where the peak related to the carbide grains could easily be identified and told from the matrix (corresponding to brighter grey levels) and from the pores (corresponding to the darkest grey levels), as illustrated in the example of Fig. 1.

X-ray diffraction (XRD: X'Pert PRO and Empyrean, PANAlytical, Almelo, NL) was performed in order to assess the phase composition of powders and coatings. Measurements were performed in Bragg-Brentano geometry over the $20° \leq 2\theta \leq 120°$ angular range, with a scanning step size of 0.017°/step, using Ni-filtered Cu-K_α radiation ($\lambda = 1.54060$ Å) focused through 0.5°-wide divergence and anti-scatter slits. The detector was a 1D solid-state array (X'Celerator, PANAlytical) with 120 s/step counting time.

Both fractions of the feedstock powder were analysed for their total carbon content by the combustion method (WC 600, LECO Corporation, St. Joseph, MI, USA). The specific surface area of the powders was determined by nitrogen adsorption using the Brunauer–Emmett–Teller (BET) theory (ASAP 2000, Micromeritics, Norcross, GA, USA). Particle porosity was measured by mercury intrusion (AutoPore IV 9500, Micrometrics). A method described by Thiele et al. [41] was used to distinguish intragranular and intergranular porosity.

The microhardness of the coatings was measured on polished cross-sections by Vickers indentation testing (Shimadzu Microhardness Tester) at three different loads of 100 gf ($\approx$ 0.1 N), 300 gf ($\approx$ 0.3 N) and 500 gf ($\approx$ 0.5 N), with a dwell time of 15 s. For each load, 20 impressions, evenly distributed in a half circle through the entire test panel, were made on each coating cross section.

Indentation fracture toughness (IFT) was measured by high-load Vickers indentations (Mitutoyo AVK C1 indenter) into the polished cross-sections of the coatings. The peak load was 5 kgf ($\approx$ 49 N) and the holding time was 10 s. Optical micrographs of the indentations (200x magnification, 2560×1920 pixel resolution) were employed in order to measure the lengths of cracks propagating from the indentation corners, using the ImageJ software [42]. Only cracks parallel to the substrate starting at the left and right tip of indents, respectively, were considered, according to the method described in [43]. The critical stress intensity (K_{IC}) was calculated from the crack lengths and indentation diagonal lengths according to the equation proposed by Niihara et al. [44], based on the Palmqvist crack model.

The Young's modulus was measured with the surface acoustic wave method (LAwave®), the details of sample preparation and measurement technique follow the previous description given by L.-M. Berger et al. [45].

The coefficient of thermal expansion (CTE) of Cr_3C_2–NiCr was measured by optical dilatometry (Horizontal Optical Dilatometer Misura® ODLT, Expert System Solutions, Modena, Italy), using free-standing slabs of $50 \times 5 \times 0.3$ mm obtained from sample JP-F (Table 1) by metallographic cutting and grinding with SiC papers, following the measurement procedure previously described by the authors [3].

2.3. Wear testing

Ball-on-disk tests (ASTM G99) were performed using a High Temperature Tribometer (Anton Paar Tritec, Peseux, Switzerland). Sintered Al_2O_3 spheres (nominal hardness HV $\approx$ 1900) were employed as counterparts, since (as explained by the authors in a previous paper [46]) alumina is chemically inert and therefore not prone to produce additional tribochemical interactions, which would confuse the interpretation of wear mechanisms. Alumina is also suitable to simulate the occurrence of wear due to sliding against hard asperities, such as foreign particles, *in-situ* developed debris, hard phases contained in the counterbody (e.g. inorganic particles and/or fibres used as reinforcement in polymer-matrix gaskets), etc.

The coatings, whose surfaces were ground and polished to *Ra* $\approx$ 0.02 µm using diamond papers and diamond slurries, were fixed to a rotating plate.

The tests were performed both at room temperature ($\approx$ 25 °C, $\approx$ 60% relative humidity) and at 400 °C. In the latter case, samples were induction heated from the base plate and their temperature was monitored (with a sampling frequency of 5 Hz) by a thermocouple in contact with their rear surface. The variability range

of the temperature, expressed as the standard deviation of the measured values, is about ± 1 °C. At least two samples were tested for each coating type.

The wear track radius was 7 mm and the sample revolution speed was set in order to achieve a relative sliding speed of 0.10 m/s; the overall sliding distance was 5000 m. The ball diameter was 6 mm and the normal load was 10 N. The same test conditions were employed by the authors in different previous studies, hence allowing the results to be compared to existing data [3,47]. The significance of such type of test is also ensured by the similarity between the morphologies of the wear tracks and the actual damage on thermal spray coatings, e.g., after sliding against gaskets in rotary seal joints, as shown in [48]. Modifying the test conditions, e.g. by further increasing the initial contact pressure, was not found to modify wear mechanisms significantly, according to a previous study by the authors [49].

The friction coefficient was determined by measuring the tangential force on the ball-holding arm with a load cell; the wear rates of the sample and of the ball counterpart were computed by normalising their volume loss over the load and sliding distance. Volume losses were determined by optical confocal profilometry (CHR150, Stil S.A., Aix en Provence, France) in the case of the sample and by optical microscopy in the case of the ball.

In order to investigate wear mechanisms, SEM inspection of wear scars, transmission electron microscope (TEM: JEM 2010, Jeol, Tokyo, Japan) observation of loose wear debris, and micro-Raman spectroscopy (LabRam, Horiba Yobin-Yvon, Villeneuve d'Ascq, France: 632.81 nm-wavelength He:Ne laser radiation) analysis of both wear scars and loose wear debris were carried out. Worn samples were also metallographically cut after embedding in a cold-curing epoxy resin (in order to avoid inducing artificial near-surface damage), ground and polished as described in Section 2.2, and observed by FEG-SEM.

Dry sand-rubber wheel (DSRW) tests were performed using a modified version of the ASTM G65 tribometer. Five samples for each coating type were tested simultaneously. As previously described [3], blocky-shaped dry quartz sand (SiO_2) with a 0.1–0.6 mm particle size was used as the abrasive. Its flow rate was 25 g/min. Sample surfaces were ground using 1200 grit SiC paper ($Ra \approx 8$ μm) before testing. During the test, the samples were pressed with a normal load of 23 N against a rotating rubber wheel with a surface speed of 1.64 m/s. The test lasted for 60 min for an overall wear distance of 5904 m. The samples were weighed every 12 min using an analytical scale with 0.001 g accuracy, in order to determine their mass loss. Worn surfaces were observed by SEM (XL40, FEI).

2.4. Statistical data treatment

The microstructural, mechanical and tribological characterisations generate a large amount of data, and it may be impractical to visualise correlations without suitable mathematical treatment. The principal component analysis (PCA) offers a convenient method to highlight the information contained in a dataset. This technique can be defined as a coordinate transformation that allows to represent data in the system that is best suited to describe its variance. Its description in this paragraph is based on the comprehensive treatise given by Jolliffe [50].

The PCA consists of applying a linear transformation that converts a set of n original variables into an equal number of derived variables, orthogonal to each other (i.e. linearly independent), chosen in such a way that the first variable accounts for the largest possible portion of the variance of the dataset, the second accounts for the largest possible portion of the residual variance, and so on. These new variables are called principal components (PCs).

Mathematically, the PCA method can be described as follows [50].

Assume an m x n matrix of experimental observations $\boldsymbol{X}=(x_{ij})$, with $i=1, \ldots, m$ and $j=1, \ldots, n$, consisting of n different variables (e.g. carbide content, hardness, toughness, etc.) measured over m points (i.e. the eight different types of coatings tested in this study).

Its n x n covariance matrix, $\boldsymbol{S}=(s_{jk})$, with $j,k=1, \ldots, n$, is defined as $s_{jk}=\frac{1}{m-1}\sum_{i=1}^{m}(x_{ij}-\overline{x_j})(x_{ik}-\overline{x_k})$, where $\overline{x_j}=<\boldsymbol{x_j}>$ and $\overline{x_k}=<\boldsymbol{x_k}>$ are the averages of the columns of $\boldsymbol{X}$ (i.e. the averages of all observations of each variable). Off-diagonal elements s_{jk} with $j \neq k$ measure how correlated the two variables $\boldsymbol{x_j}$ and $\boldsymbol{x_k}$ are; diagonal elements s_{jj} are the variances of the respective variables $\boldsymbol{x_j}$. It can be demonstrated [50] that the directions of maximum variance for the data in $\boldsymbol{X}$ are the eigenvectors $\boldsymbol{a_k}$ ($k=1, \ldots, n$) of $\boldsymbol{S}$, ordered from the largest to the smallest associated eigenvalue l_k. Denoting as $\boldsymbol{A}=(\boldsymbol{a_k})$ the matrix whose columns are the eigenvectors of $\boldsymbol{S}$ in order of decreasing eigenvalues ($l_1 > \ldots > l_k > \ldots > l_n$), the linear transformation from the original variables $\boldsymbol{X}$ to the PCs $\boldsymbol{Z}$ (whose significance is defined as above) is therefore expressed as $\boldsymbol{Z}=\boldsymbol{X} \cdot \boldsymbol{A}$.

The columns of $\boldsymbol{Z}$, i.e. the vectors $\boldsymbol{z_k}$ ($k=1, \ldots, n$) are the PCs; the eigenvectors $\boldsymbol{a_k}$, also called "loadings", are the contributions of the original variables to each PC (namely, the component a_{jk} is the contribution of the j-th variable to the k-th PC); the eigenvalues l_k are equal to the variances associated to the respective PCs.

Instead of representing each sample (i.e. each of the $m=8$ coating types) with a series of n values (i.e. its hardness, toughness, elastic modulus, wear losses, etc.), it is possible to switch to the PCs (that are linear combinations of hardness, toughness, etc.), and focus only on the first two (or three) of them whilst discarding the others. Each coating type is thus represented by two (or three) coordinates according to the selected PCs, and it can be visualised as a point in a 2-D (or 3-D) plot where the two (or three) selected PCs are the Cartesian axes.

Moreover, it is possible to define n different vectors, with components (a_{j1}, a_{j2}) or (a_{j1}, a_{j2}, a_{j3}) respectively, each representing the contributions of the j-th variable to the selected PCs. Namely, each vector shows how hardness, toughness, elastic modulus, etc., contribute to the selected PCs. By plotting these vectors on the above-mentioned 2-D or 3-D graph, interrelations between the variables can be understood. Specifically, two variables, whose vectors are parallel (antiparallel), have identical (opposite) contributions to the selected PCs; hence, they are directly proportional to each other. Two variables, whose vectors are orthogonal to each other, have completely independent contributions to the plotted PCs, hence they are unrelated to each other

It is rather easy to decide how many PCs should be retained by plotting the fraction of variance explained by each component (simply computed as $l_k/\sum_{k=1}^{n} l_k$) in a Pareto chart. Typically, it is possible to account for $>70\%$ of the variance with two or maximum three PCs. Loss of information is minimal, because the residual variance contained in the other (discarded) PCs is low.

It can be summarised, that PCs do not have a physical meaning *per se* (i.e. they are not hardness, or toughness, or modulus, …, but their linear combinations), but help devising patterns and correlations within the original data, reducing the dimensionality of the problem.

Since, in the present case, variables have different units, they are standardised as $x_{ij}^{*}=(x_{ij}-\overline{x_j})/\sqrt{s_{jj}}$ [50]. The covariance matrix $\boldsymbol{S}^{*}$ of the standardised observations matrix $\boldsymbol{X}^{*}=(x_{ij}{}^{*})$, its eigenvalues and its eigenvectors are therefore employed in the above definitions (note that $\boldsymbol{S}^{*}$ coincides with the correlation matrix of $\boldsymbol{X}$). This is done both because it is conceptually incorrect to linearly combine variables expressed in different units, and because variables with numerically greater values would have a disproportionately high influence on the principal components.

The procedure was implemented using the MATLAB (version 8.1) software.

3. Results and discussion

3.1. Structure and microstructure of the powders

Both fine (Fig. 2A,C) and coarse (Fig. 2B,D) feedstock powders contain chromium carbide grains of several micrometres in size, quite irregularly distributed in the metallic matrix. The amount of carbide grains varies between different powder particles. Many of these carbide grains also contain microcracks; some of them show very poor bonding to the surrounding matrix. These features are consistent with the general characteristics of many commercial agglomerated and sintered Cr_3C_2–NiCr powders [51].

The specific surface area is 0.21 m²/g for the fine powder (F) and 0.14 m²/g for the coarse powder (C). This difference can be attributed to the different particle size. Mercury intrusion measurements reveal nearly identical intragranular porosity for both fractions: 17.4% for the fine powder (F) and 17.5% for the coarse one (C). Both fractions show a maximum of intrusion for the intragranular porosity at an equivalent pore diameter of 4.3 μm. In the coarse powder a small second maximum at an equivalent pore diameter of 2.3 μm appears.

Significant differences are found for the total carbon content between both fractions: 9.22 wt.% for the fine powder and 10.57 wt.% for the coarse powder. It is reminded that the nominal chemical composition of the feedstock powder 75% Cr_3C_2–25% (80%Ni–20%Cr) is 70.0% Cr, 20.0% Ni and 10.0% C (in weight %).

The phase composition of both powders, evaluated from XRD patterns (detail in Fig. 3 and overviews in Fig. 4A,B, together with the XRD patterns of the coatings), comprises a f.c.c. Ni-based matrix and the Cr_3C_2 phase (JCPDF 35-804). The peaks of the Ni-based matrix are slightly shifted towards lower 2θ values, compared to those of pure Ni (JCPDF 4-850): this is most likely to reflect an increased lattice parameter due to the presence of larger Cr solute atoms. The fine powder also contains minor amounts of Cr_7C_3 (JCPDF 36-1482: see detail in Fig. 3), which is consistent with the low carbon content. This seems to be a peculiar feature of this specific type of feedstock powder. This phase is also identifiable by the presence of two slightly distinct levels of backscattered electron contrast in the carbides (Fig. 2C: labels 1 and 2). The formation of Cr_7C_3 as a second carbide phase has also been proposed during preparation of hardmetals from Cr_3C_2 and Ni powders by a conventional powder metallurgy route [52].

3.2. Structure and microstructure of the coatings

The coatings exhibit uniform microstructures (Figs. 5 and 6 for the F-and C-series, respectively), which contain some porosity between approximately 4 vol.% and 6 vol.% in all cases (Table 2). Pores are well recognisable at high magnifications and seem to

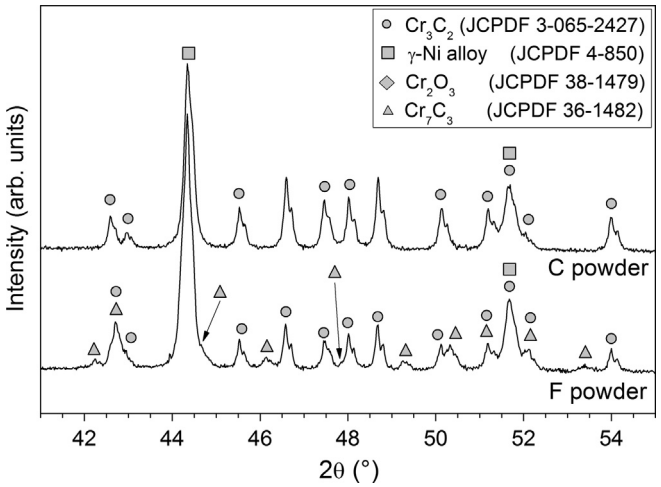

Fig. 3. XRD patterns of the fine (F) and coarse (C) feedstock powders: detail of the $41° < 2\theta < 55°$ region.

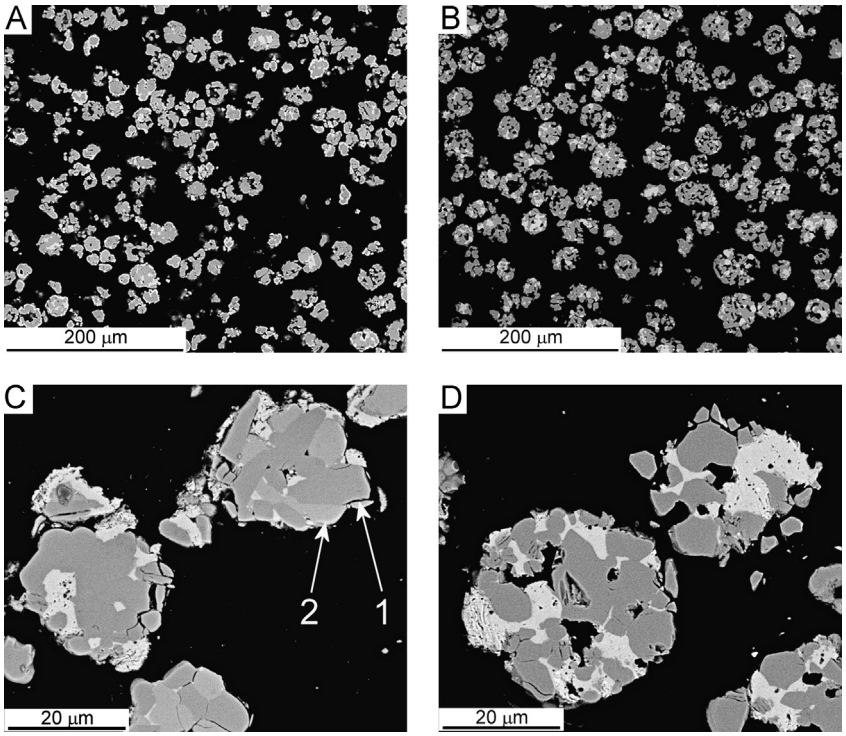

Fig. 2. SEM micrographs of powders cross-section: F powder, −38+10 μm size (A,C); C powder, −45+15 μm size (B,D). Labels 1 and 2 in panel C indicate two distinct backscatter electron contrast levels in the carbide particles of the F powder.

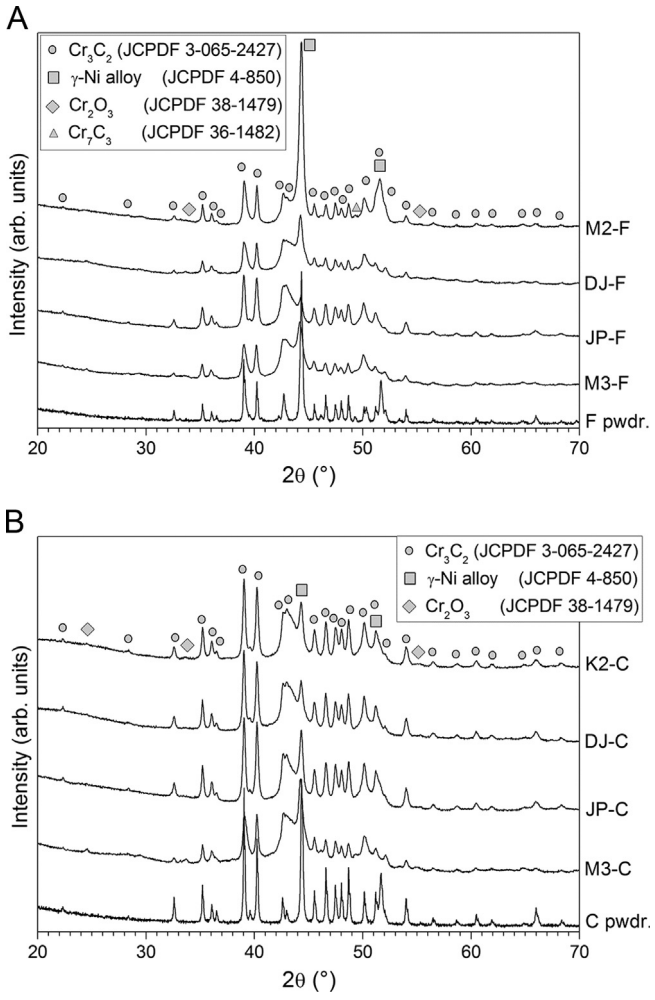

Fig. 4. XRD patterns of the fine (A) and coarse (B) feedstock powders and of the corresponding coatings.

appear quite independent of the deposition process and of the particle size of the feedstock powder, although the large experimental scatter (testified by the standard deviation values in Table 2) may prevent the recognition of slight differences between the various samples.

The powder particles described in Section 3.1, consisting of quite large carbides irregularly surrounded by the Ni-based matrix, will hardly spread out homogeneously on the substrate or the previously deposited layer [53]. The porosity observed in all coatings can therefore be due to the generation of inter-particle defects, the retention of pre-existing intraparticle porosity and the cracks of the carbide grains.

It is also interesting to note that, whilst the average carbide size is approximately the same in all samples, the total amount of retained carbides does change significantly (Table 2). On the one hand, the coatings obtained from the fine feedstock powder have systematically lower carbide content than the corresponding ones obtained by spraying the coarse powder with the same torch. On the other hand, the HVOF-sprayed coatings retained a comparable or (in the case of the samples obtained using the JP5000 torch) an even higher amount of carbides than the HVAF-sprayed ones (Table 2). These values, always <60 vol.%, are anyway significantly lower than the original carbide volume fraction in the Cr_3C_2–25 wt.%NiCr feedstock powders, which can be estimated to be $\approx$ 79 vol.% by assuming that the densities of Cr_3C_2 and Ni-20Cr are 6.68 g/cm^3 [54] and $\approx$ 8.50 g/cm^3 [55], respectively. This substantial decrease is easily observed qualitatively by comparing Figs. 2, 5 and 6.

It has to be expected that the process temperatures of the different spraying techniques will influence not only the formation and the amount of liquid phase, but also the ability of plastic deformation of the carbide grains at the moment of impact. More specifically, a previous study reported carbon loss and increased Ni content after HVOF-processing of Cr_3C_2–NiCr powders: approximately 31 wt.% and 39 wt.% Ni were found in two different coatings, both obtained from powders having a nominal Ni content of 20 wt.% [53]. The rebounding of chromium carbide grains was proposed as an important mechanism leading to the observed composition changes during spraying [53], a finding which has also been mentioned in other studies [9,38]. Carbide grains that exhibit microcracks and/or poor bonding to the matrix (Section 3.1 and Fig. 2) are likely to rebound in the present case as well. Moreover, as particular powder particles contain different amounts of carbides (Section 3.1), those with the highest carbide content can rebound more easily because of poorer plastic deformability. Rebounding is more likely in the HVAF process, due to the lower process temperature and the higher particle velocity [56,57], as observed also elsewhere [9]. Moreover, some of the fine powder particles, containing few large carbide grains bound by a very small amount of metal matrix (such as those shown in Fig. 2C), presumably have greater chance of rebounding, thus explaining the systematically smaller carbide content in the F-series samples.

In addition, carbide dissolution, carbide melting and decarburisation are also responsible for the decrease of carbide content in the coatings. Chromium carbides indeed show much lower melting or peritectic decomposition temperatures than WC or TiC [51]. Cr_3C_2 shows a peritectic decomposition at 1811 °C [58]/ 1829 °C [59], Cr_7C_3 is congruently melting at 1766 °C [58] / 1781 °C [59]. A eutectic between Cr_3C_2 and Cr_7C_3 occurs at 1727 °C [58] / 1742 °C [59]. It can anyway be mentioned that the microstructures of the present HVOF coatings exhibit much less evidence of carbide dissolution and of oxidation than those studied in [18,19,21,22,60].

Dissolution and decarburisation mechanisms are probably responsible for the particularly low (<50 vol.%) carbide content in the coatings sprayed with the gas-fuelled Diamond Jet 2700 HVOF torch (Table 2). When imaged in backscattered electron mode, the matrix phase of these coatings indeed exhibits a greater variety of greyscale shades (SEM micrographs in Figs. 5F and 6F), in comparison to all other samples (Figs. 5B,D,H and 6B,D,H). This testifies to the presence of variable amounts of dissolved Cr and C in different splats. Significant heating of some of the feedstock particles may indeed have been caused by the propane-fuelled Diamond Jet 2700 HVOF torch, where the powders, injected in the convergent nozzle section, come into contact with high-pressure combustion gases at temperatures $\geq$2700 °C [61]. The same amount of dissolution/decarburisation does not occur with liquid-fuelled HVOF torches (JP- and K2-series), where particles are injected downstream into a colder, expanded gas jet (the temperature of which typically lies between 1700 °C and 2200 °C [62]).

XRD patterns (Fig. 4) indicate that the coatings retain the same qualitative phase composition of the respective feedstock powders, comprising the f.c.c. Ni-based matrix (with slightly shifted peaks), the Cr_3C_2 carbide phase, and, in the case of the F-series samples, minor amounts of the Cr_7C_3 carbide as well. In the XRD patterns of the coatings, however, the diffraction peaks of the Ni-based matrix become broader than they are in the patterns of the corresponding powders, and their intensity decreases relative to the peaks of Cr_3C_2. This result, which may apparently seem inconsistent with the reduced Cr_3C_2 content in the coatings, could indicate amorphisation and/or formation of substantial lattice defects in the matrix, as a possible consequence of its severe

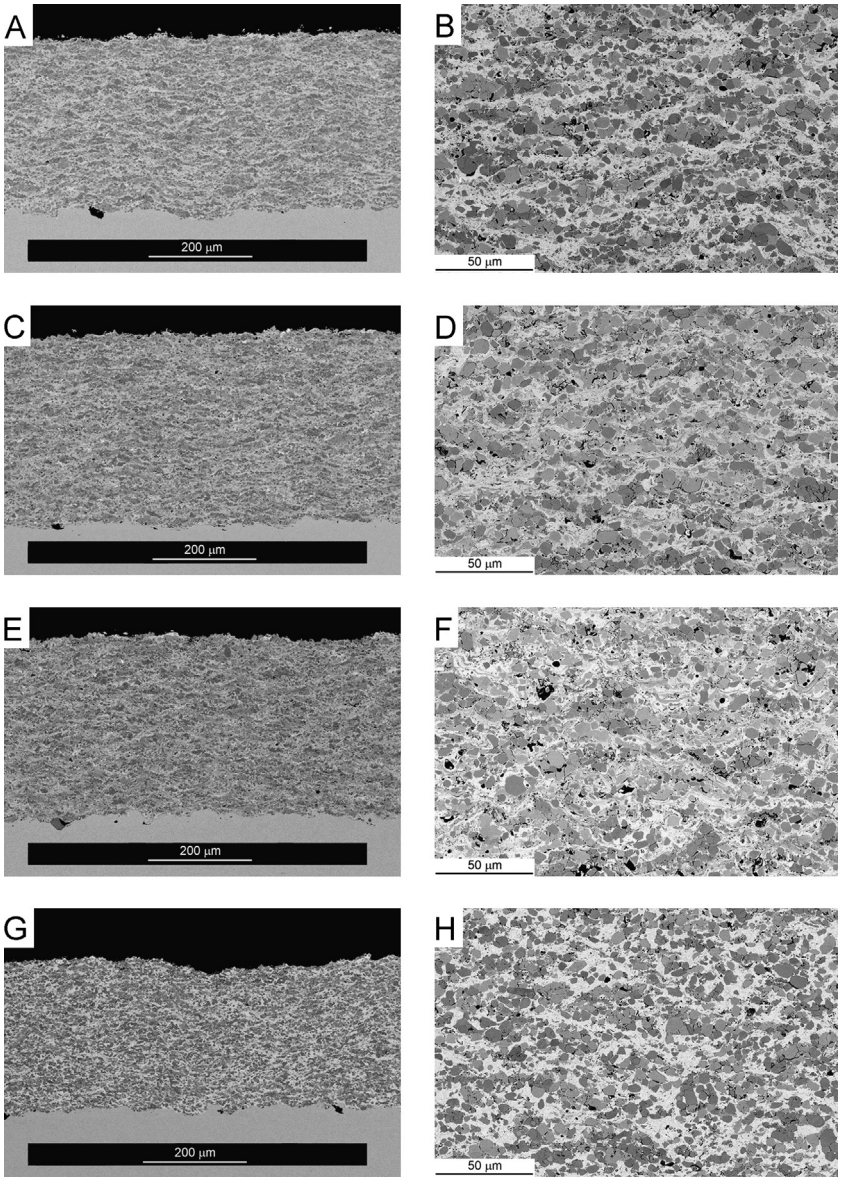

Fig. 5. Cross-sectional SEM micrographs of samples M3-F (A,B), JP-F (C,D), DJ-F (E,F), M2-F (G,H): low-magnification overviews (A,C,E,G) and high-resolution FEG-SEM details (B,D,F,H), representative of the micrographs employed for image analysis purposes.

deformation upon impact, of melt quenching (mainly in HVOF processes), and/or of the presence of excess Cr and C from chromium carbide dissolution. Matrix phases consisting of a solid solution super-saturated with respect to Cr and C were also reported in references [9,18,19,21,22,60], and the presence of an amorphous fraction in the matrix was clearly shown by TEM analyses [20]. The intensities of the diffraction peaks are therefore not representative of the overall amount of matrix phase, i.e. XRD patterns are not a means to estimate the relative amount of carbides and matrix in the coatings. This justifies the use of the image analysis technique instead of XRD pattern fitting for this purpose.

The only exception to the above considerations is the M2-F coating (Fig. 4A), where the matrix peaks remain sharper and more intense, similar to the pattern of the feedstock powder. This suggests that, on the one hand, melting of the matrix was very limited or absent during the M2-HVAF spraying process, and that, on the other hand, its plastic deformation upon impact onto the substrate was not as extensive as in the M3-HVAF deposition. The crystal grain structure of the M2-F sample is indeed highlighted by the electron channelling contrast in high-resolution backscattered-electrons FEG-SEM micrographs (Fig. 7A), whilst it disappeared in the M3-F sample (Fig. 7B).

Some very weak peaks in the XRD patterns of Fig. 4 might be ascribed to Cr_2O_3: it can therefore be estimated that the coatings (both HVOF and HVAF ones) contain some oxides in amounts comparable to the XRD detection limit (1–2%). These are not clearly seen in the micrographs of Figs. 5 and 6, but become perceivable as small, dark spots in the detailed views of Fig. 7. Accordingly, recent results have shown that HVOF and HVAF processes differ much less than expected in terms of carbon loss and oxygen uptake for Cr_3C_2–NiCr [37].

In general, the metallurgical interactions between the carbide grains and the metallic matrix are very complex and require further work for a full understanding.

3.3. Mechanical and tribological properties of the coatings

3.3.1. Statistical analysis

In order to link the coating microstructures (Table 2), their mechanical properties (hardness, elastic modulus and indentation

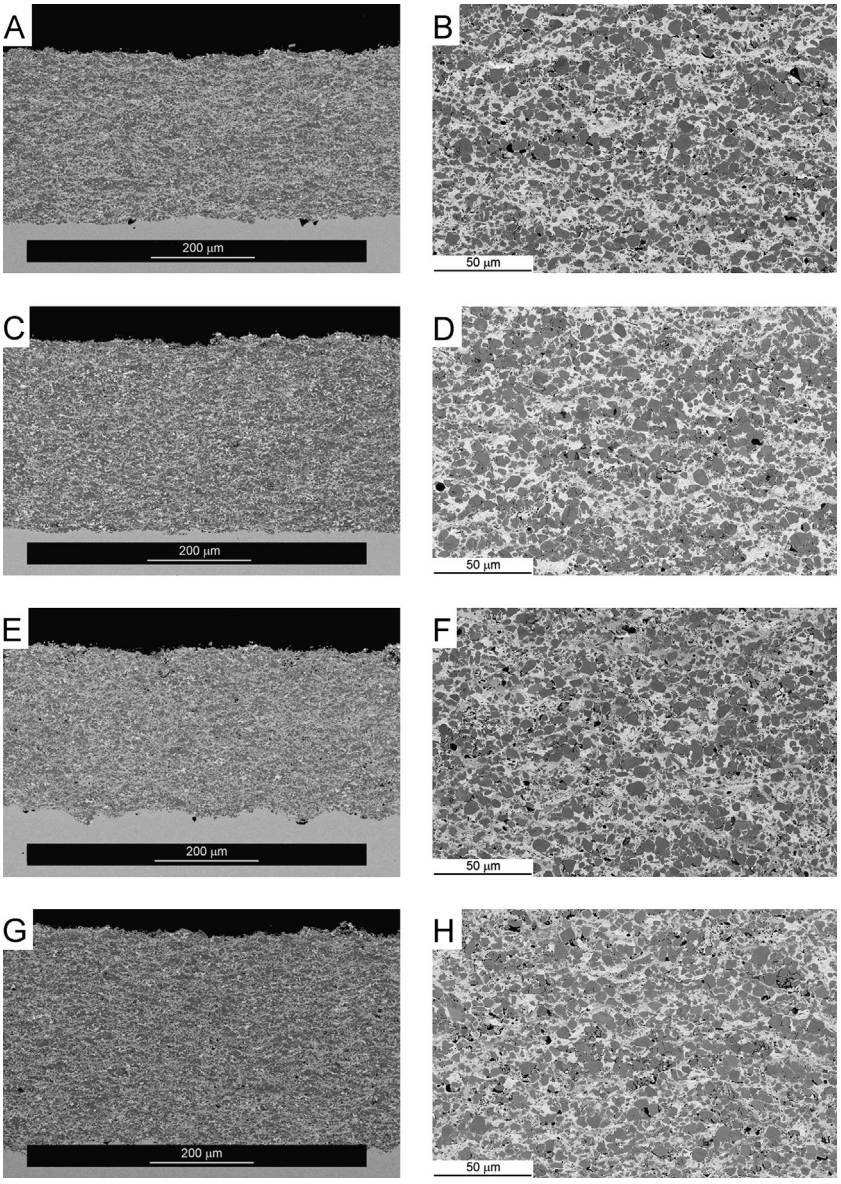

Fig. 6. Cross-sectional SEM micrographs of samples M3-C (A,B), JP-C (C,D), DJ-C (E,F), K2-C (G,H): low-magnification overviews (A,C,E,G) and high-resolution FEG-SEM details (B,D,F,H), representative of the micrographs employed for image analysis purposes.

Table 2
Summary of microstructural parameters of all coatings: porosity, carbide content, carbide particle size (average ± standard deviation).

Sample	Porosity (vol.%)	Carbides content (vol.%)	Carbides size (μm)
M3-F	4.1 ± 1.9	50.3 ± 1.0	1.2 ± 0.5
JP-F	3.9 ± 1.3	53.0 ± 2.7	1.5 ± 0.5
DJ-F	3.5 ± 2.2	48.5 ± 3.0	1.2 ± 0.6
M2-F	6.2 ± 1.7	54.9 ± 1.7	1.6 ± 0.6
M3-C	3.9 ± 1.2	53.4 ± 1.7	1.4 ± 0.6
JP-C	6.3 ± 3.2	57.1 ± 0.9	1.6 ± 0.6
DJ-C	5.3 ± 2.1	49.3 ± 0.9	1.6 ± 0.6
K2-C	4.0 ± 1.7	52.9 ± 1.4	1.4 ± 0.6

fracture toughness), summarised in Table 3, and the performances under abrasive wear (mass losses after the DSRW test, Fig. 8A) and sliding wear conditions (sliding wear rates, Fig. 8B,C), the principal component analysis (PCA) technique was applied as described in Section 2.4. The same method was accordingly employed by the authors in order to interpret the wear behaviour of WC-CoCr coatings as well [3].

Porosity was discarded from the analysis due the previously mentioned lack of significant differences between the samples within error range (Section 3.2). A total of $n=9$ variables were therefore considered, thus analysing an $m=8 \times n=9$ matrix of experimental observations (see Section 2.4). The matrix was standardised by subtracting the mean of each variable and by dividing over the respective standard deviation, so as to obtain dimensionless numbers that can be logically compared to each other, avoiding disproportionate effects from numerically large values, as explained at the end of Section 2.4.

The Pareto chart shows that the 1st, 2nd and 3rd principal components (PCs) account for almost 90% of the overall variance (Fig. 9A). Data can therefore be represented using these PCs only, which provides a significant simplification of the problem. Instead of having 9 separate variables (which could not be graphically visualised on a single plot), only three variables (the 1st, 2nd and 3rd PCs) are selected, allowing a 3D plot to be obtained (Fig. 9B). Points represent each of the $m=8$ samples in the reference system consisting of the selected PCs, and vectors

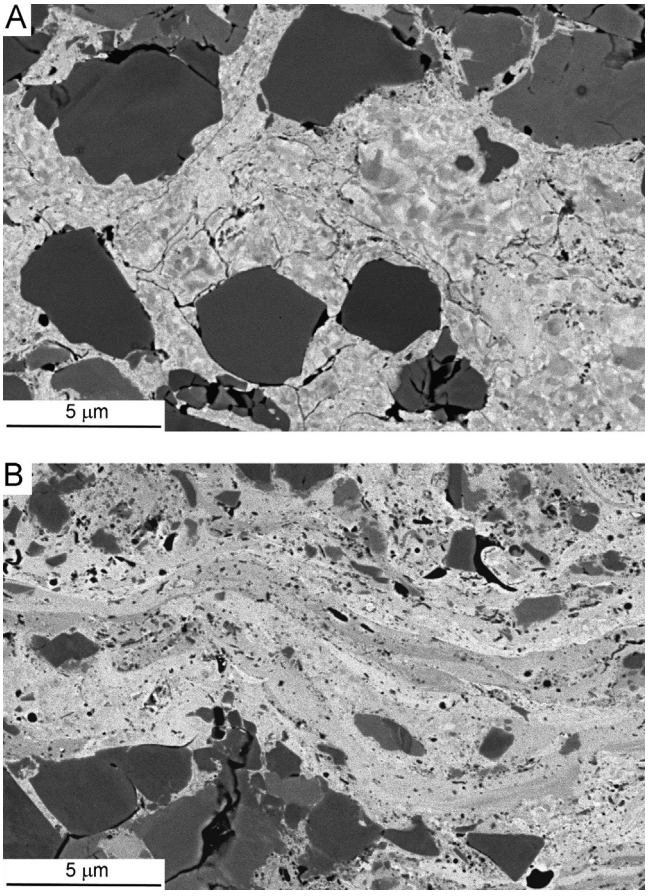

Fig. 7. High-resolution FEG-SEM micrographs highlighting the matrix structure in the M2-F (A) and M3-F (B) samples.

Table 3
Summary of the mechanical parameters of all coatings: microhardness, elastic modulus and indentation fracture toughness (average ± standard deviation).

Sample	$HV_{0.1}$	$HV_{0.3}$	$HV_{0.5}$	E [GPa]	K_{IC} [MPa m$^{1/2}$]
M3-F	1021 ± 110	875 ± 79	922 ± 44	185.5 ± 1.5	3.62 ± 0.35
JP-F	952 ± 158	859 ± 85	835 ± 54	172.5 ± 0.2	3.75 ± 0.45
DJ-F	919 ± 161	933 ± 20	885 ± 61	170.7 ± 1.9	4.13 ± 0.33
M2-F	641 ± 129	613 ± 68	626 ± 40	136.3 ± 1.7	2.26 ± 0.24
M3-C	981 ± 142	879 ± 94	895 ± 94	203.0 ± 2.5	4.60 ± 0.62
JP-C	842 ± 175	709 ± 88	736 ± 72	174.9 ± 0.4	3.59 ± 0.48
DJ-C	900 ± 198	797 ± 105	772 ± 107	174.8 ± 0.5	4.06 ± 0.49
K2-C	1008 ± 160	868 ± 115	854 ± 64	193.0 ± 0.6	4.13 ± 0.40

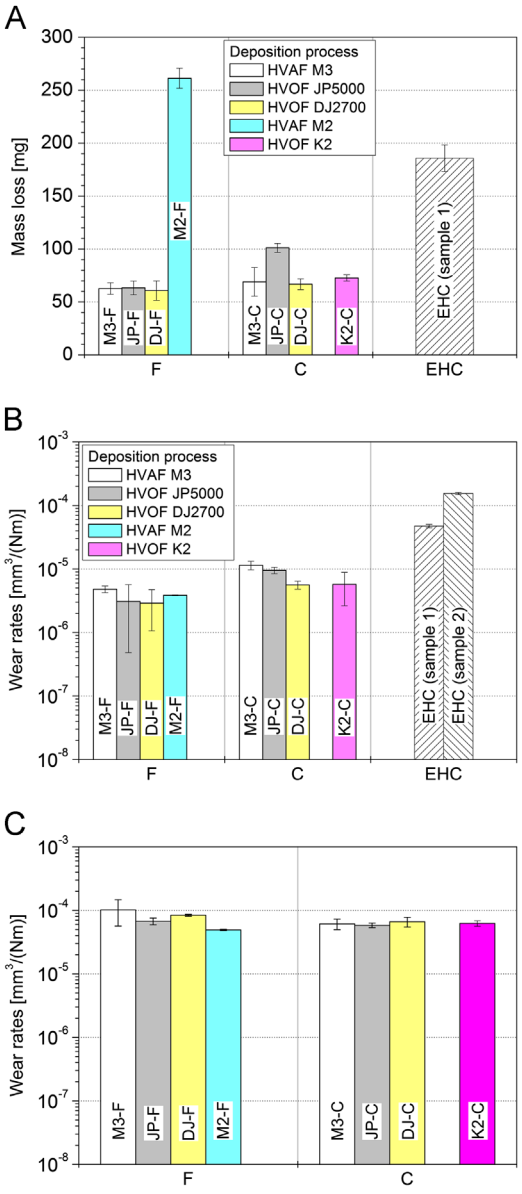

Fig. 8. Mass losses recorded after dry sand-rubber wheel abrasion testing (A) and wear rates measured after ball-on-disk testing at room temperature (B) and at 400 °C (C). Thermal spray coatings are labelled according to Table 1. EHC = electrolytic hard chromium coatings.

provide the contributions of each of the $n=9$ variables to those PCs, as illustrated in Section 2.4.

From those contributions, some important considerations can be drawn:

(1) The elastic modulus and the indentation fracture toughness are closely related to each other.
Both of these properties were indeed measured by macro-scale techniques (acoustic wave propagation and high-load indentation testing, respectively); therefore, both are primarily controlled by long-range features, namely by the inter-lamellar cohesive strength. An analogous observation was made for elastic modulus and fracture toughness measurements on WC-CoCr coatings [3].

(2) All hardness values ($HV_{0.1}$, $HV_{0.3}$ and $HV_{0.5}$) are closely related to each other and they are only partly related to indentation fracture toughness and elastic modulus. Hardness, indeed, bears some relation to intra-lamellar scale features (i.e. features, whose length scale is smaller than the size of the lamellae produced by impact deformation of the original powder particles). Specifically, with indentation loads of 100–500 gf, the probed volume covers one or few lamellae; hence, the results depend partly on long-range inter-lamellar cohesion and partly on short-range intra-lamellar features.
Most of the $HV_{0.1}$ values are slightly higher than $HV_{0.3}$ and $HV_{0.5}$ ones (Table 3), consistent with the general finding that, in thermally sprayed materials, the measured hardness decreases with increasing load until a plateau is attained at about 300 gf [63]. The intralamellar contribution to $HV_{0.1}$ is indeed slightly higher, because of the smaller indentation volume. The difference, however, is only a minor one and the overall significance of the values does not change. Nano-indentation would have been needed to probe a sufficiently small material volume,

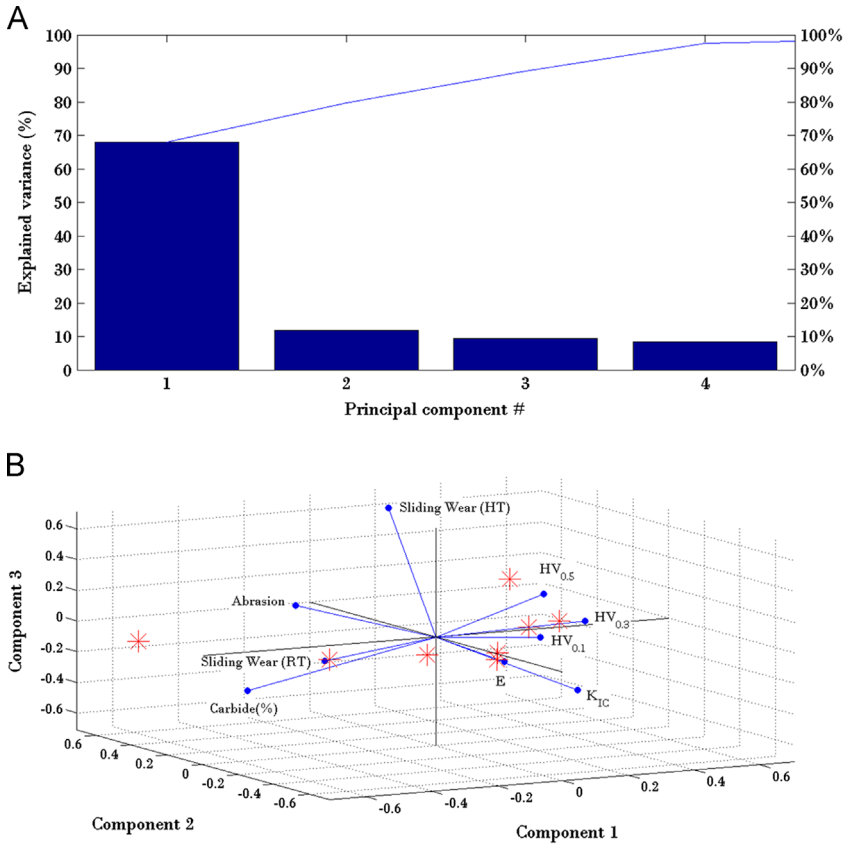

Fig. 9. Results of PCA on the microstructural, mechanical and tribological data (Table 2 and 3, Fig. 8): (A) Pareto chart and (B) plot representing the contributions of each variable (lines) and the coordinates of the data points (stars) according to the 1st, 2nd and 3rd PCs.

reflecting intra-lamellar features only [38,64,65]; however, such analysis is outside the scope of this paper. Elastic modulus and toughness, by contrast, are not much dependent on intra-lamellar features, such as the carbide content (the respective vectors in Fig. 9B being nearly orthogonal), in accordance with the observation at point I.

Interestingly, hardness tends to increase as the carbide content decreases, the respective vectors in Fig. 9B being anti-parallel. Coatings deposited using the finer powder are indeed generally harder (Table 3), though possessing systematically lower carbide content (Table 2 and Section 3.2), which is easily understood by comparing the data for the couples M3-F / M3-C, JP-F / JP-C, DJ-F / DJ-C. The amount of defects within the carbide grains and their cohesion to the surrounding matrix clearly play an important role on hardness. It can be proposed that, on the one hand, the porosity of the coarse powder particles (Section 3.1 and Fig. 2) is less effectively decreased by impact deformation in each of the spray processes. On the other hand, enhanced particles rebounding using the fine powder (Section 3.2) means only well-bonded carbide grains are retained, improving the intra-lamellar strength of the material.

Since this systematic recurrence is not true for fracture toughness and elastic modulus (the latter would instead seem to be higher for coatings deposited with the coarse powder), it is inferred that the difference is due to intra-lamellar rather than inter-lamellar factors.

Sample M2-F is an exception to the previous considerations, as it provides low hardness values at all indentation loads. More specifically, its values of hardness, fracture toughness and elastic modulus are the lowest among all samples. This reflects very poor inter-lamellar cohesion, which is probably related to the insufficient deformation of the powder particles upon impact, in accordance with the previous observations (Section 3.2).

(3) The abrasive mass loss and the sliding wear rate at room temperature bear little relation to each other, and the sliding wear rate at high temperature is definitely unrelated to both, as its vector in Fig. 9B is almost orthogonal to the others. This suggests a substantial difference between the wear mechanisms; it also means that the wear resistances under distinct tribological conditions have different dependencies on the microstructural and mechanical properties.

It is also seen in Fig. 9B that, compared to the abrasion mass loss and to the sliding wear rate at room temperature, the sliding wear rate at high temperature (400 °C) gives the least contribution to the 1st and 2nd PCs and the largest to the 3rd one. The 1st PC is the one carrying most of the variance (Fig. 9A), and the points representing the coordinates of the 8 sample types in the PCs reference system are substantially lined up along the 1st PC axis (Fig. 9B). This means the coatings differ less in terms of sliding wear rates at 400 °C than they do for the room-temperature wear rate and for the abrasion mass loss. This can be qualitatively appreciated from Fig. 8.

For each wear test, these features are discussed in detail in the forthcoming sections.

3.3.2. *Dry sand-rubber wheel abrasion testing*

SEM observations of wear scars (Fig. 10) indicate that wear proceeds through large-scale abrasive grooving (grooves being several micrometres wide, Fig. 10A,C: arrows) and through the pull-out of splats, splat fragments or of individual Cr_3C_2 grains (Fig. 10B,D: circles). Higher cohesive strength both at inter- and at intra-lamellar levels can clearly restrain all of these phenomena by

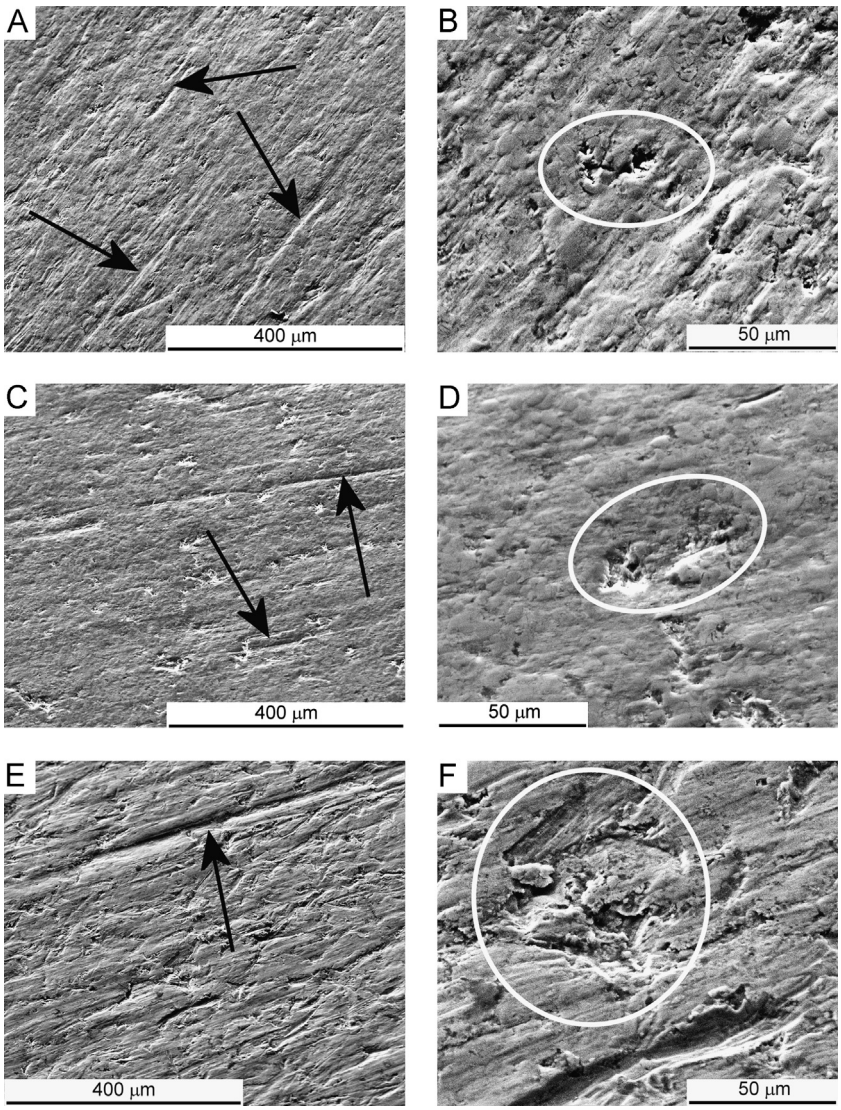

Fig. 10. Secondary electron SEM micrographs of the wear scars produced on samples M3-F (A,B), DJ-F (C,D) and M2-F (E,F) after dry sand-rubber wheel testing. Arrows: abrasive grooves; circles: pull-outs.

limiting the penetration of abrasive particles and by hindering the pull-out of material portions.

This explains why abrasion mass loss decreases almost linearly with increasing elastic modulus and indentation fracture toughness, i.e. the properties which measure inter-lamellar cohesion strength (Section 3.3.1), and also tends to decrease with increasing hardness, which measures both inter- and intra-lamellar strength (Section 3.3.1). These relations are seen from Fig. 9B: the vector representing the abrasion mass loss is nearly anti-parallel to those of elastic modulus and indentation fracture toughness and reasonably anti-parallel to those of the hardness values, indicating linear proportionality (Section 3.3.1).

In particular, the abrasive wear resistance improves slightly but systematically when changing from coarse to fine feedstock powder (Fig. 8A: compare samples M3-F, JP-F, DJ-F to samples M3-C, JP-C, DJ-C respectively), following the same trend of hardness (Table 3). The higher intra-lamellar cohesive strength conferred to the coatings by the finer feedstock powder (as discussed previously) can indeed restrain the pull-outs of individual carbides and of splat fragments.

The M2-F coating clearly exhibits the widest, deepest abrasive grooves (Fig. 10E: arrows), as its lower hardness cannot prevent the penetration of abrasive particles. It also shows larger pull-outs (Fig. 10F: circle), most of which probably involve entire splats because of the lower cohesive strength.

Apart from sample M2-F, the mass loss of the coatings is significantly lower than that of a reference electroplated hard chromium sample, previously reported in [3].

3.3.3. *Ball-on-disk sliding wear testing – room temperature*

The dry sliding wear rates of the Cr_3C_2–NiCr coatings produced at room temperature (Fig. 8B) are around or slightly below 10^{-5} $mm^3/(Nm)$, which is consistent with the values generally reported in the literature for such coatings tested under similar conditions [29,30,66]. Quite comparable wear rates were also found by some of the present authors both in dry sliding against Al_2O_3 counterbodies and in self-mated contact conditions, using a specially designed ball-on-disk tribometer [32,33].

The Cr_3C_2–NiCr coatings are significantly more wear resistant than two reference electroplated hard chromium coatings, deposited onto the same substrates at an industrial facility (Fig. 8B).

In this case, wear proceeds by three distinct mechanisms:

(1) Abrasive grooving (Fig. 11: some of the most clearly recognisable grooves are marked by arrows), which affects both the matrix and the chromium carbide grains. The grooves are

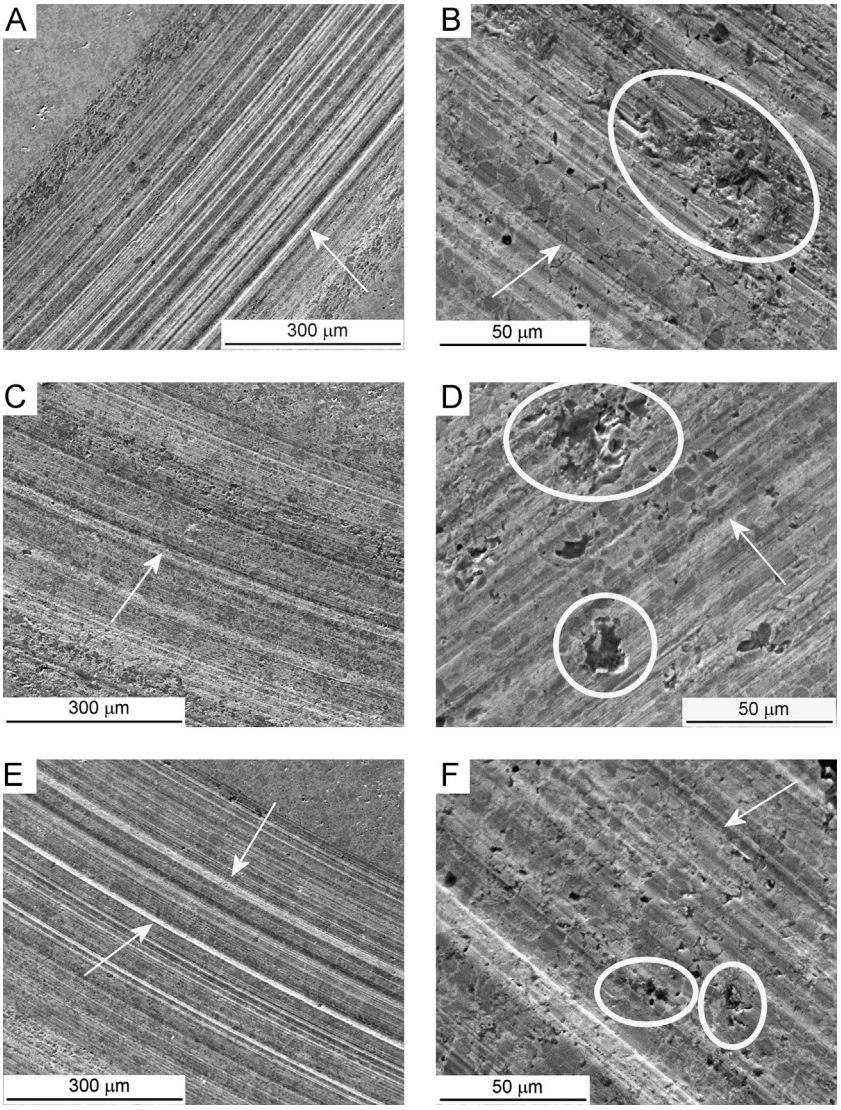

Fig. 11. SEM micrographs of the wear scars produced after ball-on-disk testing of Cr_3C_2–NiCr coating samples M3-F (A,B), JP-F (C,D), DJ-F (E,F). Arrows: abrasive grooves; circles: pull-outs.

produced by hard alumina asperities and/or by wear debris particles, which can freely move between the mating bodies or stick to the counterbody surface. Grooves are much shallower and narrower than those seen in rubber wheel abrasion testing (compare to Fig. 10), indicating that the abrading asperities and debris particles are much smaller than the quartz particles employed in the abrasive wear tests. The coating material is therefore loaded on a much smaller length scale than in rubber wheel abrasion, mainly corresponding to the intra-lamellar scale. Inter-lamellar cohesion probably plays a less significant role on abrasive grooving processes in this case. For this reason, the sliding wear rate is more closely related to hardness (nearly anti-parallel vectors) and less closely related to indentation fracture toughness and elastic modulus than dry particles abrasion is (Section 3.3.2).

(2) Cracking, fragmentation and pull-out of individual carbide grains, which is particularly well seen in magnified views, such as those of Fig. 11B,C,F (some pull-outs are circled in the micrographs), and in the detail of Fig. 12A (cracks in a carbide grain are shown by arrows). Cross-sectional views also reveal surface and sub-surface cracks propagating across the carbide grains or along their interface with the metal matrix, leading to pull-outs (Fig. 12B: see circled areas).

The phenomenon is however confined to a very shallow depth, i.e. it takes place at the intra-lamellar scale: this is once again consistent with the close relation between sliding wear at room temperature and hardness, which depends, at least in part, on intra-lamellar cohesion (Fig. 9B). Pull-outs are favoured by the retention of carbide grains with cracks and/or poor cohesion to the matrix (as discussed in Section 3.1). Consistent with the observations set forth when discussing hardness in Section 3.3.1, coatings retaining a larger amount of carbide grains with cracks and poor cohesion to the matrix do not perform well under sliding wear conditions at room temperature. Namely, the controlling factor for sliding wear resistance is not the sheer number of carbide grains, at least as long as their amount remains within a reasonably small interval, but rather the amount of defects within these grains and their cohesion to the surrounding matrix.

Recently, it has been shown that plasma treated feedstock powders, and consequently the coatings produced thereof, do

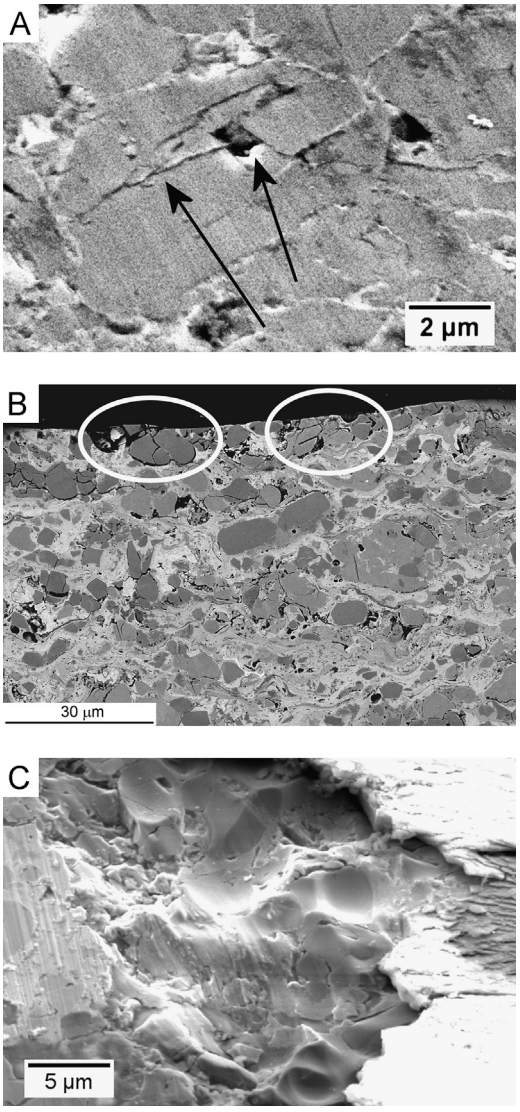

Fig. 12. Details of the wear tracks: (A) microcracks (see arrows) in a carbide grain in sample JP-C, (B), microcracked carbides and pull-outs (circles) in the cross-section of sample JP-F, adhesive/delaminative tearing on sample JP-C.

not contain carbide grains with cracks [37]. Also the use of alternative preparation routes of Cr_3C_2 would allow to prevent such cracks.

(3) Delamination (Fig. 12C), with a morphology suggesting adhesive wear. Accordingly, a layer of transferred material (Fig. 13) covers the alumina counterbodies, which exhibit negligible wear loss. Delamination is probably dependent on inter- and intra-lamellar cohesion together.

As a term of comparison, a similar combination of adhesive wear and of abrasion by trapped debris particles was also observed for thermally sprayed Cr_3C_2–NiCr coatings in ball-on-disk sliding against an alumina counterbody in [24].

On the other hand, since inter-lamellar factors are somewhat less important than in dry particle abrasion testing, the M2-F coating, which possesses much lower inter-lamellar cohesion, is anyway comparable to all other coatings under sliding wear conditions.

Sliding between the coating surface and the transferred material on the surface of the counterbody (Fig. 13) causes high friction. After some running-in, the friction coefficient values of the Cr_3C_2–NiCr coatings reached up to 0.70–0.75 (Fig. 14). This is

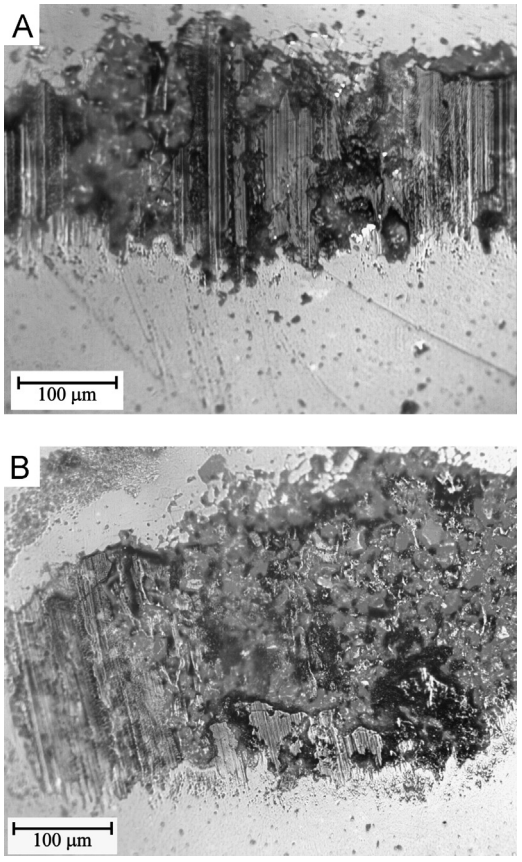

Fig. 13. Optical micrographs of the wear scars produced on the alumina counterbody after ball-on-disk testing against Cr_3C_2–NiCr coatings: M3-C (A) and JP-C (B).

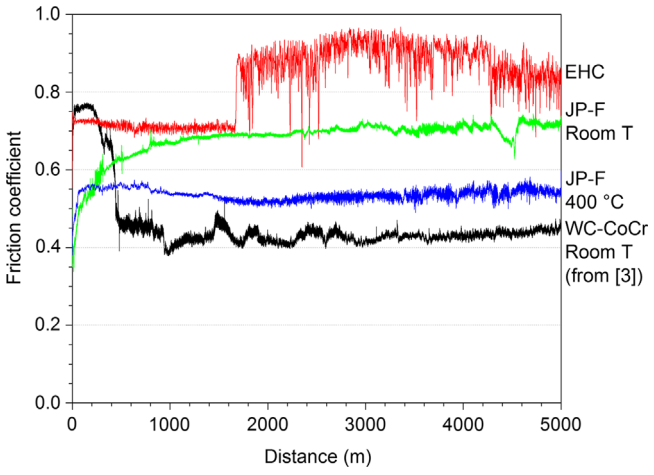

Fig. 14. Friction coefficient measured during ball-on-disk dry sliding wear tests performed on sample JP-F at room temperature and at 400 °C, compared to values recorded in [3] at room temperature for an electroplated hard chromium reference and for a WC–CoCr coating.

consistent with the value of ≈ 0.7 shown in [24] for a Cr_3C_2–NiCr coating/Al_2O_3 ball couple sliding under analogous load and speed settings. Similar values were also reported in [32,34]. The WC–CoCr coatings tested under the same conditions in the previous work [3] produced comparatively lower friction coefficients of 0.45–0.50, as no adhesion and no material transfer to the counterbody was reported in that case.

High friction also implies significant flash heating. Whilst this flash heating is not enough to produce a continuous oxidised

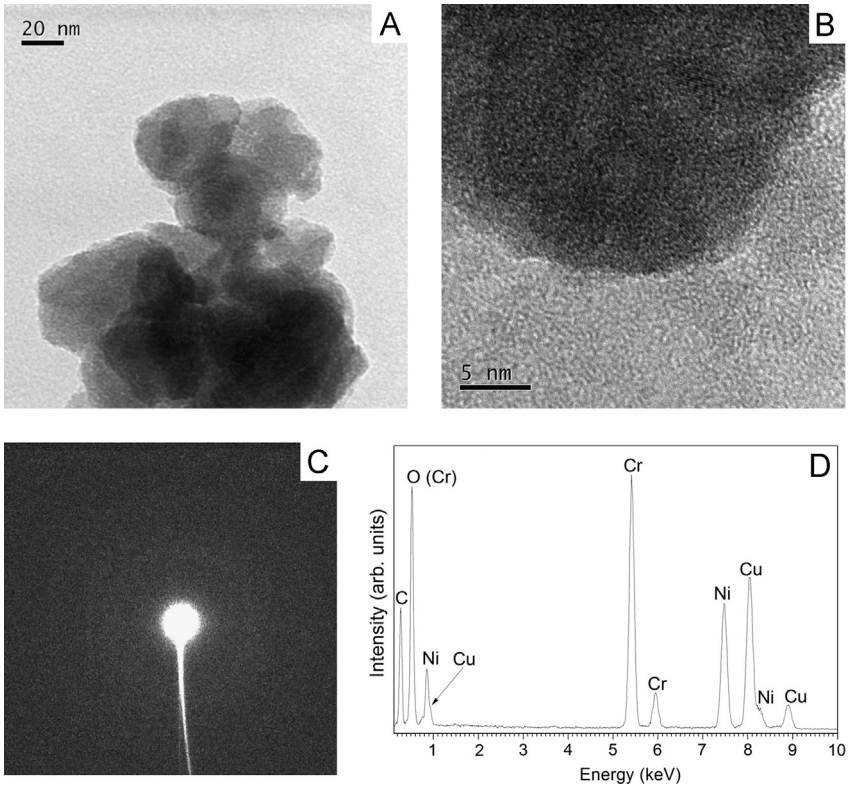

Fig. 15. Bright-field TEM micrographs of the loose wear debris collected after ball-on-disk testing on sample M3-C at room temperature (A,B), selected area diffraction pattern collected on the area seen in panel B (C), and representative EDX spectrum (D).
Note: the EDX peak of Cu in panel D comes from the contribution of the TEM sample holder.

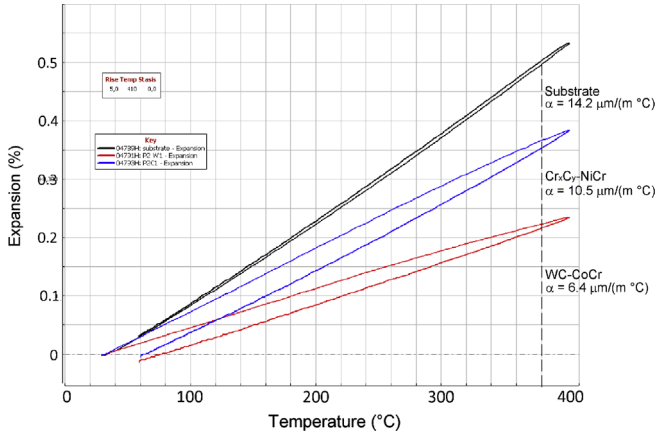

Fig. 16. Optical dilatometer measurement on a free-standing Cr_3C_2–NiCr coating sample, compared to a WC–CoCr coating and to the steel substrate (the latter are both taken from [3]).

tribo-film on the coating surface (it was accordingly shown in [24] that a continuous oxidised tribo-film, capable of lowering friction and wear, only appears at sliding speeds of about 1 m/s), it is sufficient to oxidise the debris particles and part of the transferred material. This is inferable from the presence of darker clusters on the transfer layer in Fig. 13 and confirmed by the TEM analysis of the loose debris collected on the sample after the wear test. This indeed consists of aggregates of amorphous nanometric particles (TEM micrographs in Fig. 15A,B and SAED pattern in Fig. 15C) rich in oxygen (EDX spectrum in Fig. 15D).

This oxidised debris can certainly contribute to the previously described small-scale abrasive grooving, so that each wear mechanism corroborates to the other ones.

3.3.4. *Ball-on-disk sliding wear testing – 400 °C*

At 400 °C, the wear rates of all Cr_3C_2–NiCr coatings are comprised between $5x10^{-5}$ $mm^3/(Nm)$ and 10^{-4} $mm^3/(Nm)$ (Fig. 8C), consistent with the results of various oscillating [66] and rotating [32,33] ball-on-disk tests performed against a variety of hard counterbodies (including Si_3N_4 [66] and Al_2O_3 [32]) as well as in self-mated conditions [32,33]. The values are approximately one order of magnitude higher than those at room temperature (compare to Fig. 8B).

Wear is more severe than that of WC–CoCr coatings tested under the same conditions in [3] (the wear rates of which were slightly above 10^{-7} $mm^3/(Nm)$). The WC–CoCr coatings, however, exhibited a strong tendency to micro- and macro-cracking at this temperature [3], whereas none of the Cr_3C_2-NiCr samples showed cracks after the wear testing at 400 °C.

From the curves in Fig. 16, it is indeed inferred that the thermal expansion coefficient of Cr_3C_2–NiCr in the 30 °C–380 °C temperature range is $10.5x10^{-6}$ $°C^{-1}$, i.e. it is significantly higher than that of WC–CoCr and comparatively closer to that of the steel substrate (equal to $14.2x10^{-6}$ $°C^{-1}$, from Fig. 16). This CTE consistently lies between those of Cr_3C_2–20%Ni ($\approx 10.3x10^{-6}$ $°C^{-1}$) and Cr_3C_2–40% Ni ($\approx 11.3x10^{-6}$ $°C^{-1}$), as reported in [11] for the 30 °C – 400 °C range. It also falls in between the values of $10.30x10^{-6}$ $°C^{-1}$ and of $12.21x10^{-6}$ $°C^{-1}$ reported in [67] for two Cr_3C_2–25%NiCr coatings obtained from different feedstock powders. In [3], using the composite beam model (as described in [68]), the thermal expansion mismatch stress arising at 400 °C in a WC–CoCr coating deposited onto a planar steel substrate was estimated to be $\approx +600$ MPa. With a 350 µm-thick Cr_3C_2–NiCr coating on a 8 mm-thick steel substrate, the same equations (with the CTE values given above) indicate that the thermal expansion mismatch stresses are of about +175 MPa (with a coating Young's modulus of $\approx$ 170 GPa, Table 3), i.e. more than three times lower than the former value.

In some cases, Cr_3C_2–NiCr hardmetals could therefore be a safer choice than WC–CoCr ones for the protection of steel substrates at 400 °C, due to the much lower CTE mismatch. They also offer the advantage of producing lower friction coefficient ($\approx$ 0.55, as shown in Fig. 14) than WC–CoCr ($\geq$ 0.8 [3]) at that temperature. However, this comes at the cost of much higher wear rates ($\approx 1x10^{-4}$ mm^3/(Nm) for Cr_3C_2–NiCr – Fig. 8C – against $\approx 1x10^{-7}$ mm^3/(Nm) for WC–CoCr [3]). The WC-$(W,Cr)_2C$-Ni composition, studied by the authors in [47], also provides somewhat better CTE matching to standard steel substrates (its CTE at 400 °C being $8.70x10^{-6}$ $°C^{-1}$ [67]). Though not as well matched as Cr_3C_2–NiCr, previous research did not highlight cracking problems with WC-$(W,Cr)_2C$-Ni onto steel substrates at high temperatures as well [47]. However, the friction coefficient of WC-$(W,Cr)_2C$-Ni sliding against sintered Al_2O_3 at 400 °C, under the same test conditions, was reported to be $\approx$ 0.74 [47], i.e. this material cannot match the low friction of Cr_3C_2–NiCr.

These considerations show that there is still significant room for future research aiming to devise hardmetal compositions that can overcome such limitations, providing optimal high-temperature wear protection while avoiding excessively large thermal expansion mismatch with common substrate materials.

The data in Fig. 8C also shows that, at 400 °C, the use of the fine feedstock powder does not provide systematically better sliding wear resistance, differently from the room temperature results previously described in Section 3.3.2. To the contrary, in some cases, the opposite is true (compare samples M3-F and M3-C, DJ-F and DJ-C). The PCA results in Fig. 9B accordingly show that samples rank very differently in terms of sliding wear resistance at room temperature and at 400 °C. In the latter case, indeed, abrasive grooving dominates the sliding wear behaviour (Fig. 17: some grooves are marked by arrows). Fracturing and pull-out of carbides are not seen as frequently as at room temperature (Fig. 17). Cross-sectional views show that they are not entirely suppressed (Fig. 18: see marked features), but their influence on the overall volume loss is clearly smaller than that of the extensive abrasive grooving seen in Fig. 17. The considerations made in Section 3.3.3 concerning the systematically poor performance of coatings retaining a larger amount of poorly-bonded carbide grains are therefore no more valid in these conditions. The reason for such deep change may reside in thermal softening, which could have lessened the brittleness of the coatings, improving the carbides-matrix cohesion.

Interestingly, abrasive grooves seem larger in the samples deposited with the Diamond Jet HVOF torch (see Fig. 17E,F for sample DJ-F), whilst the other samples (see Fig. 17A-D for samples M3-F and JP-F: the same considerations also hold for all other samples) exhibit more numerous and smaller abrasive grooves and

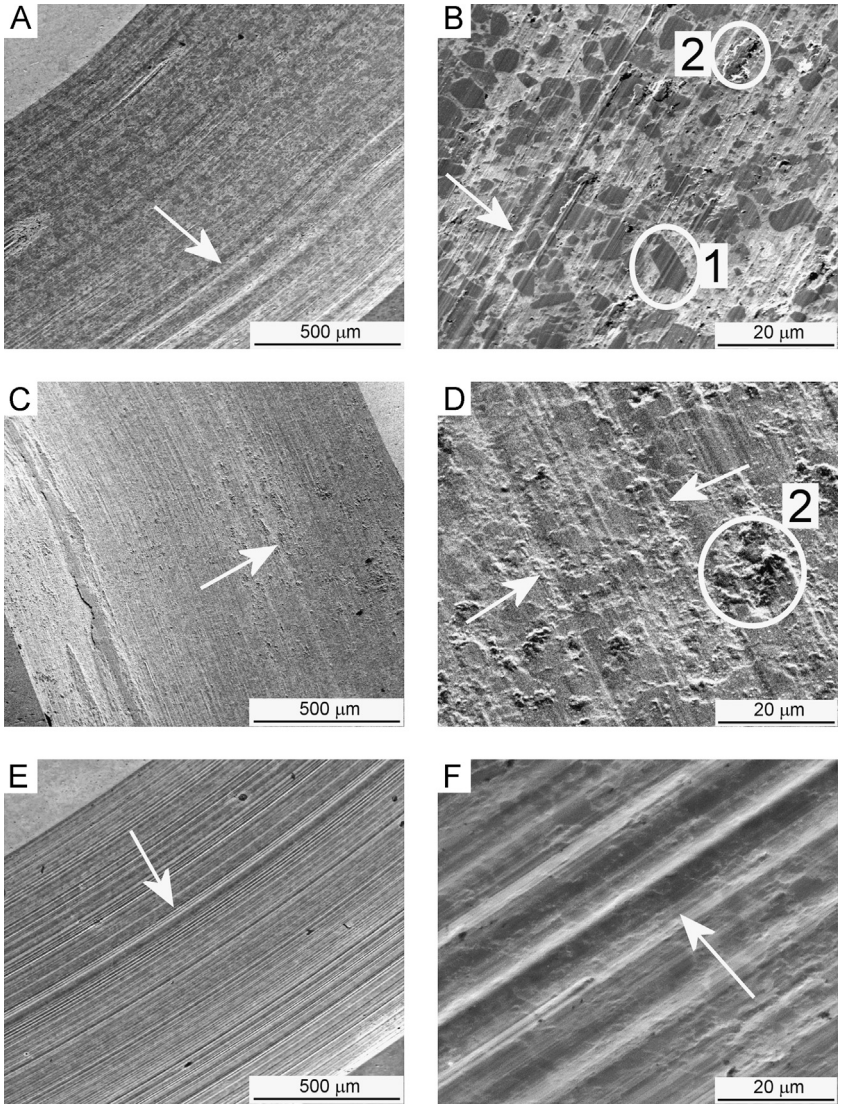

Fig. 17. SEM micrographs of the wear scars produced after ball-on-disk testing at 400 °C on samples M3-F (A,B), JP-F (C,D) and DJ-F (E,F). Arrows: abrasive grooves; label 1: protruding carbides; label 2: oxide clusters.

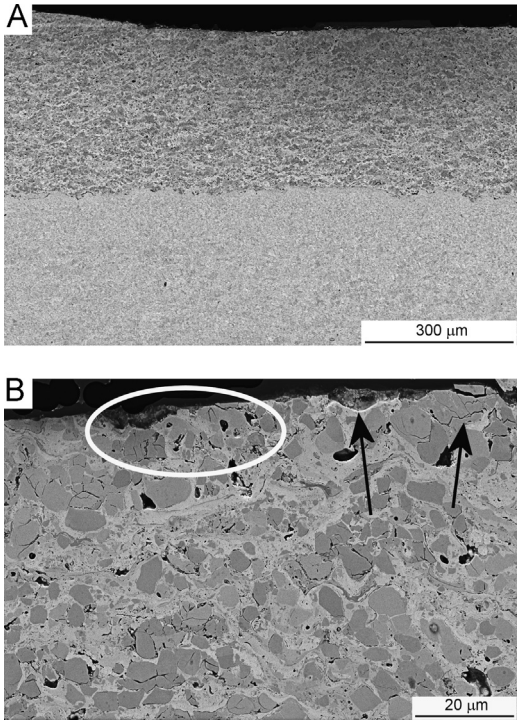

Fig. 18. Cross-sectional SEM micrographs (A: overview; B: detail) of the wear scar produced on sample JP-F after ball-on-disk sliding wear testing at 400 °C. Circle and arrows indicate some carbide cracking and pull-out.

some oxide clusters (label 2). Nonetheless, this did not result in major differences between the wear rates (Fig. 8C).

Previous studies showed that long-term isothermal holding of Cr_3C_2–NiCr coatings at higher temperatures (between 650 °C and 900 °C) embrittled the matrix by carbide re-precipitation [19,21,22,40]. At 400 °C, by contrast, such re-precipitation is not occurring to a perceivable degree; indeed, the cross-sectional micrograph in Fig. 18B reveals no secondary carbide grains appearing in the matrix, and no change in phase composition is detectable through XRD patterns (Fig. 19). This is in agreement with other recent results [38].

The ball counterbody still undergoes negligible wear loss (Fig. 20), and it becomes covered by part of the wear debris generated by the coating. Interestingly, this debris is less oxidised in the case of the DJ-F and DJ-C samples (see the metallic shine of the transfer layer in Fig. 20B) than it is for all other samples (compare to Fig. 20A), consistent with the differences between the wear scar morphologies of the respective coatings (Fig. 17).

The oxidised debris, as observed by TEM analysis of the residual loose fraction in the case of JP-C, consists of agglomerated nano-sized particles (Fig. 21A,B). Significant oxidation is confirmed by EDX analyses (Fig. 21D). Unlike the debris collected at room temperature, these particles possess a fine crystalline structure, which is clearly seen through SAED patterns (Fig. 21C).

The Raman spectra of the debris (those of samples DJ-F and JP-C are shown in Fig. 22), apart from the peak of the $NiCr_2O_4$ spinel phase at $\approx 680\ cm^{-1}$ [69], also exhibit the characteristic broad bands of graphite at about $1350\ cm^{-1}$ and $1575\ cm^{-1}$ [70]. Graphite clusters may have been formed by thermo-mechanical alteration of the carbide particles during high-temperature sliding, including the release of graphitic C as Cr is combined with oxygen, and/or the interaction between Cr_3C_2 and Ni within the debris particles. These clusters probably account for the remarkable decrease in friction coefficient (Fig. 14) compared to that measured at room temperature.

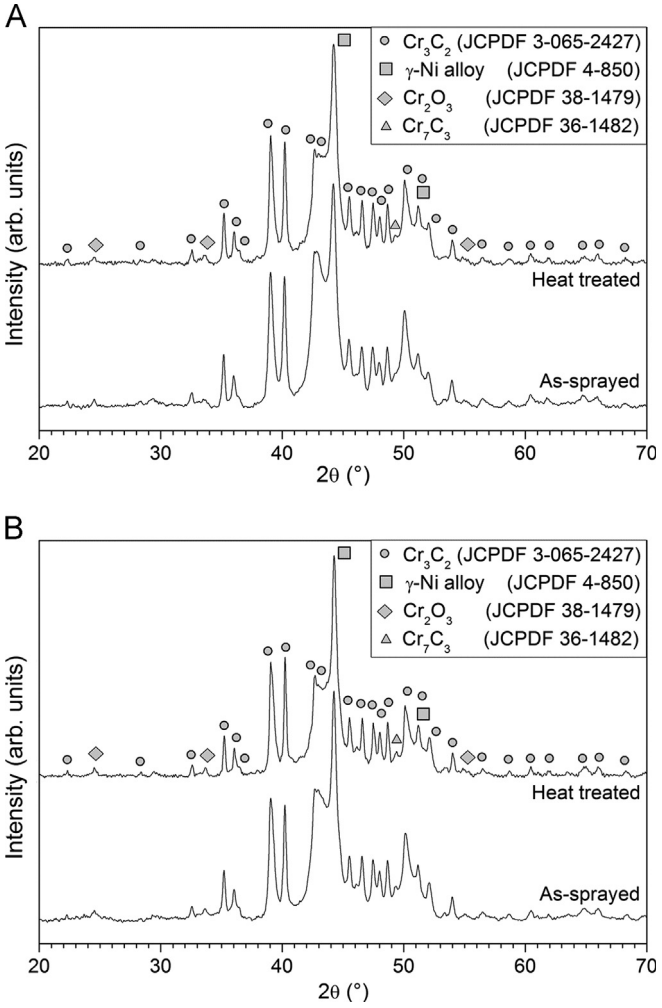

Fig. 19. XRD patterns of samples M3-F (A) and DJ-F (B) before and after holding at 400 °C for ≈ 14 h during the high-temperature sliding wear test.

4. Conclusions

The tribological properties of eight different Cr_3C_2–NiCr coatings representative of the existing state-of-the art, deposited by HVOF- and HVAF-spraying techniques using one feedstock powder with two distinct particle size distributions, were systematically assessed under sliding and abrasive wear conditions. The following conclusions can be drawn:

- The fine and the coarse feedstock powder show similar characteristics regarding their intragranular porosity, but show a significant difference of the total carbon content. The lower total carbon content of the fine fraction is responsible for the existence of lower carbide Cr_7C_3.
- All coatings contain lower amounts of Cr_3C_2 particles than the feedstock powders, with some liquid-fuelled HVOF samples attaining higher carbide contents than the HVAF-sprayed ones do. The loss of Cr_3C_2 is primarily ascribed to the preferential rebounding of Cr_3C_2 grains and of Cr_3C_2-rich powder particles during high-velocity impact, and seems to be favoured by the use of the finer feedstock powder. Some dissolution and decarburisation of Cr_3C_2 grains also takes place, especially when using the gas-fuelled Diamond Jet HVOF torch.
- Each deposition technique produces harder coatings when the finer feedstock powder is used.

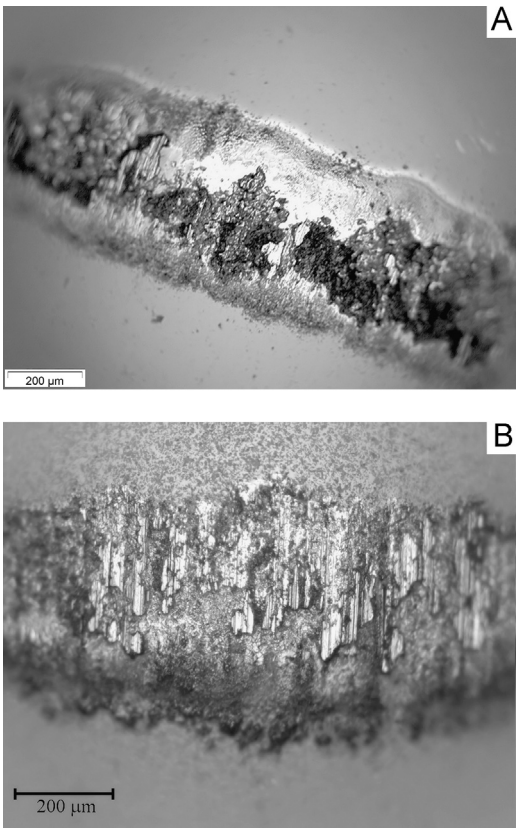

Fig. 20. Optical micrographs of the ball surfaces after dry sliding wear testing of samples M3-F (A) and DJ-F (B) at 400 °C.

- Dry particle abrasion involves coarse abrasive grooving and pull-out of coating fragments. The performance of the coatings therefore depends on their cohesive strength both at the inter-lamellar and at the intra-lamellar level. Principal component analysis accordingly reveals that the abrasion mass loss is closely related to the mechanical properties reflecting long-range inter-lamellar cohesion (such as fracture toughness and elastic modulus), and partly related to micro-hardness, which depends both on inter- and on intra-lamellar cohesion.

For this reason, the harder coatings obtained with the fine feedstock powder are systematically more wear resistant than the corresponding ones obtained from the coarse powder.

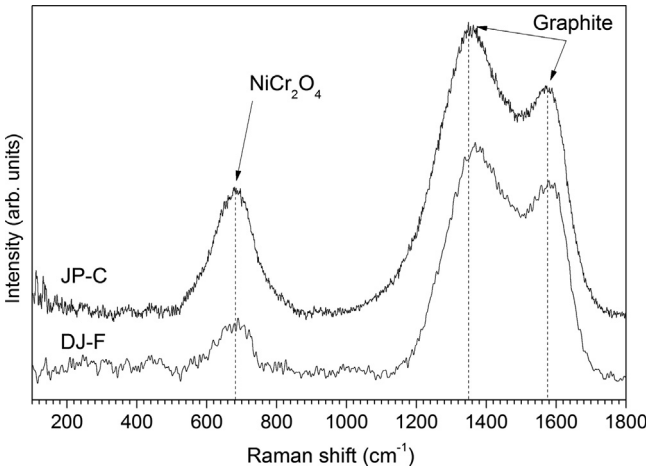

Fig. 22. Representative micro-Raman spectrum of the loose wear debris collected after ball-on-disk sliding wear testing of samples DJ-F and JP-C at 400 °C.

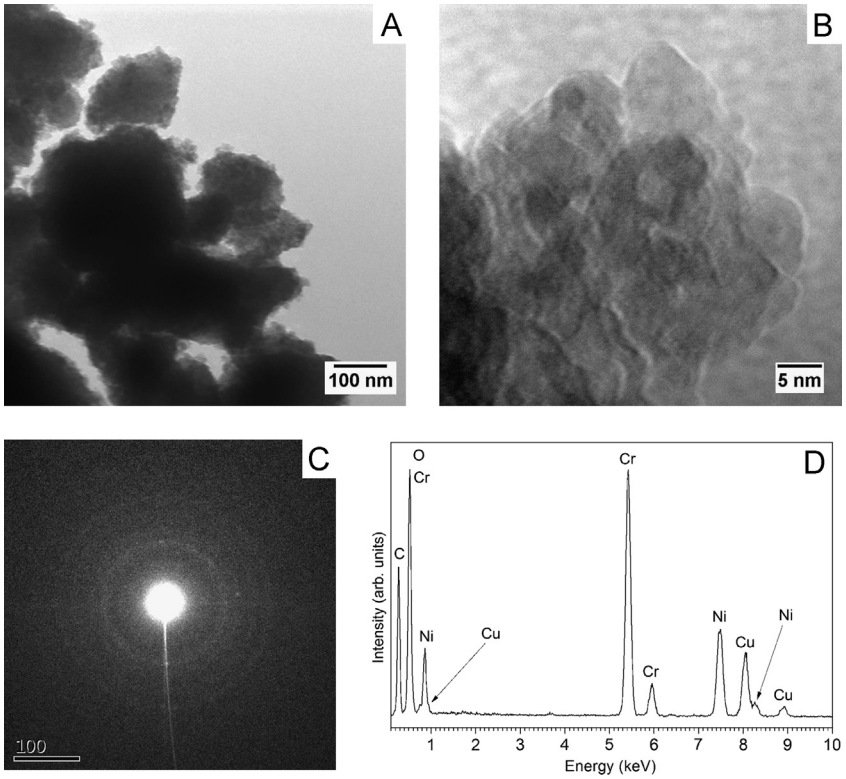

Fig. 21. Bright-field TEM micrographs (A,B) of the loose wear debris collected after ball-on-disk sliding wear testing of sample JP-C at 400 °C, with corresponding SAED pattern (C) and EDX spectrum (D). Note: the EDX peak of Cu in panel D comes from the contribution of the TEM sample holder.

The sample sprayed with the M2-HVAF torch, by contrast, has very poor abrasion resistance due to its low inter-lamellar cohesion, probably related to insufficient particle deformation at impact.

- Sliding wear at room temperature involves shallower abrasive grooving, carbide pull-outs and limited adhesive wear contributions. Most of these mechanisms take place at the intra-lamellar level; hence, sliding wear at room temperature bears some relation to hardness, as the latter is also affected by intra-lamellar strength.
  In any case, the fine feedstock powder provides slightly more wear-resistant coatings than the coarse one, due to a stronger matrix-carbide cohesion inside the lamellae after spraying.
  It is also noted that coatings containing more numerous carbide grains are not necessarily more sliding wear resistant at room temperature, since it is the amount of defects in the carbide grains and their cohesion to the matrix, rather than the number of carbide grains, which controls the wear resistance.
  Wear rates, comprised between $5x10^{-6}$ $mm^3/(Nm)$ and $1x10^{-5}$ $mm^3/(Nm)$, are significantly lower than those of electroplated hard chromium, but larger than those of WC-CoCr coatings.
- At 400 °C, wear rates are comprised between $5x10^{-5}$ and $1x10^{-4}$ $mm^3/(Nm)$, i.e. they increase by one order of magnitude compared to the room-temperature values. Friction coefficients, however, decrease from ≈0.7 at room temperature to ≈0.5 at 400 °C. This is probably related to the observed formation of graphite clusters within the wear debris at this temperature.
  Wear is dominated by abrasive grooving, whereas fracturing and pull-out of carbides are mitigated, probably because of thermal softening.
- None of the Cr_3C_2–NiCr coatings cracks at 400 °C, since the thermal expansion coefficient of Cr_3C_2–NiCr in the 30 °C – 400 °C temperature range ($11.08x10^{-6}$ °C^{-1}) is relatively close to that of the steel substrate ($14.23x10^{-6}$ °C^{-1}). Cr_3C_2-NiCr is therefore a safer choice than WC-CoCr for sliding wear protection of steel substrates at 400 °C, and also produces lower friction, although the latter material is significantly more wear resistant.

Acknowledgements

Many thanks to Dr. Benno Gries, and Dr. Olav Norheim (H.C. Starck GmbH, Laufenburg, Germany) for providing the feedstock powders and the JP5000-HVOF sprayed coatings for this research. The authors are also grateful to Ing. Chiara Venturelli (Expert Lab Service S.r.l., Modena, Italy) for performing the optical dilatometer measurements and to Mr. Roberto Puschmann (Fraunhofer IWS) for spraying of the M2-F and K2-C coatings.

References

[1] L.-M. Berger, R. Puschmann, J. Spatzier, S. Matthews, Potential of HVAF spray processes, Therm. Spray Bull. 6 (2013) 16–20.
[2] K. Tao, X. Zhou, H. Cui, J. Zhang, Microhardness variation in heat-treated conventional and nanostructured NiCrC coatings prepared by HVAF spraying, Surf. Coat. Technol. 203 (2009) 1406–1414.
[3] G. Bolelli, L.-M. Berger, T. Börner, H. Koivuluoto, L. Lusvarghi, C. Lyphout, et al., Tribology of HVOF- and HVAF-sprayed WC–10Co4Cr hardmetal coatings: a comparative assessment, Surf. Coat. Technol. 265 (2015) 125–144.
[4] L. Fedrizzi, L. Valentinelli, S. Rossi, S. Segna, Tribocorrosion behaviour of HVOF cermet coatings, Corros. Sci. 49 (2007) 2781–2799.
[5] K. Luer, The erosion-oxidation behavior of HVOF Cr_3C_2-NiCr cermet coating, Wear 174 (1994) 177–185.
[6] S. Matthews, B. James, Review of thermal spray coating applications in the steel industry: part 1-hardware in steel making to the continuous annealing process, J. Therm. Spray Technol. 19 (2010) 1267–1276.
[7] G.-J. Yang, C.-J. Li, S.-J. Zhang, C.-X. Li, High-temperature erosion of HVOF sprayed Cr_3C_2-NiCr coating and mild steel for boiler tubes, J. Therm. Spray Technol. 17 (2008) 782–787.
[8] Š. Houdková, F. Zahálka, M. Kašparová, L.M. Berger, Comparative study of thermally sprayed coatings under different types of wear conditions for hard chromium replacement, Tribol. Lett. 43 (2011) 139–154.
[9] L.-M. Berger, R. Trache, F.-L. Toma, S. Thiele, J. Norpoth, L. Janka, Development of cost-effective hardmetal coating solutions for high-temperature applications, Part two, Therm. Spray Bull. 8 (2015), in press.
[10] Y. Ding, T. Hussain, D.G. McCartney, High-temperature oxidation of HVOF thermally sprayed NiCr–Cr_3C_2 coatings: microstructure and kinetics, J. Mater. Sci. 50 (2015) 6808–6821.
[11] M. Antonov, I. Hussainova, J. Pirso 4th Interational Conference "Industrial Engineering - Innovation as Competitive Edge for SME", in: J. Papstel, B. Katalinic (Eds.), Chromium Carbide Based Cermets as the Wear Resistant Materials, DAAAM Estonia, Tallinn, Estonia, 2004, pp. 169–172.
[12] S. Singh, H.S. Sidhu, B.S. Sidhu, Characterisation and corrosion-erosion behaviour of carbide based thermal spray coatings, J. Miner. Mater. Charact. Eng. 11 (2012) 569–586.
[13] S. Thiele, K. Sempf, K. Jaenicke-Roessler, L.-M. Berger, J. Spatzier, Thermophysical and microstructural studies on thermally sprayed tungsten carbide-cobalt coatings, J. Therm. Spray Technol. 20 (2011) 358–365.
[14] F. Otsubo, H. Era, K. Kishitake, T. Uchida, Properties of Cr_3C_2-NiCr cermet coating sprayed by high power plasma and high velocity oxy-fuel processes, J. Therm. Spray Technol. 9 (2000) 499–504.
[15] G.Y. Lai, Evaluation of sprayed chromium carbide coatings for gas-cooled reactor applications, Thin Solid Films 53 (1978) 343–351.
[16] J.R. Lindgren, W.R. Johnson, Friction and wear behavior of chromium carbide coatings, Surf. Coat. Technol. 32 (1987) 249–260.
[17] P. Vuoristo, K. Niemi, A. Mäkelä, T. Mäntylä, Abrasion and erosion wear resistance of Cr_3C_2-NiCr coatings prepared by plasma, detonation and high-velocity oxyfuel spraying, in: C.C. Berndt, S. Sampath (Eds.), Thermal Spray Industrial Applications: Proceedings of the 7th National Thermal Spray Conference, ASM International, Materials Park, Ohio, USA, 1994, pp. 121–126.
[18] S. Matthews, B. James, M. Hyland, High temperature erosion of Cr_3C_2-NiCr thermal spray coatings - the role of phase microstructure, Surf. Coat. Technol. 203 (2009) 1144–1153.
[19] S. Matthews, B. James, M. Hyland, The role of microstructure in the mechanism of high velocity erosion of Cr_3C_2-NiCr thermal spray coatings: part 2-Heat treated coatings, Surf. Coat. Technol. 203 (2009) 1086–1093.
[20] J.K.N. Murthy, K. Satya Prasad, K. Gopinath, B. Venkataraman, Characterisation of HVOF sprayed Cr_3C_2-50(Ni20Cr) coating and the influence of binder properties on solid particle erosion behaviour, Surf. Coat. Technol. 204 (2010) 3975–3985.
[21] S. Matthews, B. James, M. Hyland, High temperature erosion-oxidation of Cr_3C_2-NiCr thermal spray coatings under simulated turbine conditions, Corros. Sci. 70 (2013) 203–211.
[22] S. Matthews, B. James, M. Hyland, The role of microstructure in the mechanism of high velocity erosion of Cr_3C_2-NiCr thermal spray coatings: part 1-As-sprayed coatings, Surf. Coat. Technol. 203 (2009) 1086–1093.
[23] M. Roy, A. Pauschitz, R. Polak, F. Franek, Comparative evaluation of ambient temperature friction behaviour of thermal sprayed Cr_3C_2–25(Ni20Cr) coatings with conventional and nano-crystalline grains, Tribol. Int. 39 (2006) 29–38.
[24] M. Mohanty, R.W. Smith, M. De Bonte, J.P. Celis, E. Lugscheider, Sliding wear behavior of thermally sprayed 75/25 Cr_3C_2/NiCr wear resistant coatings, Wear 198 (1996) 251–266.
[25] F. Rastegar, D.E. Richardson, Alternative to chrome: HVOF cermet coatings for high horse power diesel engines, Surf. Coat. Technol. 90 (1997) 156–163.
[26] J.M. Guilemany, N. Espallargas, P.H. Suegama, A.V. Benedetti, Comparative study of Cr_3C_2-NiCr coatings obtained by HVOF and hard chromium coatings, Corros. Sci. 48 (2006) 2998–3013.
[27] J.M. Guilemany, N. Espallargas, J. Fernández, P.H. Suegama, A.V. Benedetti, High-velocity oxyfuel Cr_3C_2-NiCr replacing hard chromium coatings, J. Therm. Spray Technol. 14 (2005) 335–341.
[28] W. Zorawski, S. Kozerski, Scuffing resistance of plasma and HVOF sprayed WC12Co and Cr_3C_2-25(Ni20Cr) coatings, Surf. Coat. Technol. 202 (2008) 4453–4457.
[29] D. Poirier, J.-G. Legoux, R.S. Lima, Engineering HVOF-sprayed Cr_3C_2-NiCr coatings: the effect of particle morphology and spraying parameters on the microstructure, properties, and high temperature wear performance, J. Therm. Spray Technol. 22 (2013) 280–289.
[30] G. Bolelli, B. Bonferroni, J. Laurila, L. Lusvarghi, A. Milanti, K. Niemi, et al., Micromechanical properties and sliding wear behaviour of HVOF-sprayed Fe-based alloy coatings, Wear 276-277 (2012) 29–47.
[31] M. Roy, A. Pauschitz, J. Wernisch, F. Franek, The influence of temperature on the wear of Cr_3C_2–25(Ni20Cr) coating—comparison between nanocrystalline grains and conventional grains, Wear 257 (2004) 799–811.
[32] L.-M. Berger, M. Woydt, S. Saaro, Reib-/Gleitverschleiß von thermisch gespritzten Hartmetallschichten, in: R. Suchentrunk (Ed.), Jahrbuch Oberflächentechnik, Vol. 63, Eugen G. Leuze Verlag, Bad Saulgau, Germany, 2007, pp. 242–267.
[33] L.M. Berger, M. Woydt, S. Saaro, Comparison of self-mated hardmetal coatings under dry sliding conditions up to 600 °C, Wear 266 (2009) 406–416.
[34] L.-M. Berger, M. Woydt, S. Zimmermann, H. Keller, G. Schwier, R. Enžl, et al. Tribological behavior of HVOF-sprayed Cr_3C_2-NiCr and TiC-based coatings under high-temperature dry sliding conditions, in: Thermal spray 2004:

Advances in Technology and Application - Proceedings of the International Thermal Spray Conference, ASM International, Materials Park OH, USA, 2004, pp. 468–477.
[35] C.J. Li, K. Sonoya, G.-C. Ji, Y.-Y. Wang, Effect of powder type on the relationship between spray parameters and properties of HVAF sprayed Cr_3C_2-NiCr coatings, in: C. Coddet (Ed.), Thermal Spray Meeting the Challenges of the 21st Century - Proceedings of the 15th International Thermal Spray Conference, ASM International, Materals Park, OH, USA, 1998, pp. 287–292.
[36] S. Wirojanupatump, P. Shipway, D. McCartney, The influence of HVOF powder feedstock characteristics on the abrasive wear behaviour of Cr_xC_y–NiCr coatings, Wear 249 (2001) 829–837.
[37] L.-M. Berger, R. Trache, F.-L. Toma, S. Thiele, J. Norpoth, L. Janka, Development of cost-effective hardmetal coating solutions for high-temperature applications, part one: feedstock powders, cost-effectiveness and coating properties, Therm. Spray Bull. 8 (2015) 126–136.
[38] L. Janka, J. Norpoth, R. Trache, L.-M. Berger, Influence of heat treatment on the abrasive wear resistance of a Cr_3C_2-NiCr coating deposited by an ethene-fuelled HVOF spray process, Surf. Coat. Technol. 291 (2016) 444–451.
[39] Habonim Industrial Valves and Actuators – Petrochemical industry – Valves, actuators and special solutions catalogue. ⟨http://www.habonim.com/pdf/ind_catalogs/Petrocheamical/Petrochemical_M.pdf⟩ (accessed October 25, 2015).
[40] L. Vernhes, D.A. Lee, D. Poirier, D. Li, J.E. Klemberg-Sapieha, HVOF coating case study for power plant process control ball valve application, J. Therm. Spray Technol. 22 (2013) 1184–1192.
[41] S. Thiele, R.B. Heimann, L. Berger, M. Herrmann, M. Nebelung, T. Schnick, et al., Microstructure and properties of thermally sprayed silicon nitride-based coatings, J. Therm. Spray Technol. 11 (2002) 218–225.
[42] M.D. Abràmoff, P.J. Magalhães, S.J. Ram, Image processing with ImageJ, Biophotonics Int. 11 (2004) 36–41.
[43] M.M. Lima, C. Godoy, P.J. Modenesi, J.C. Avelar-Batista, A. Davison, A. Matthews, Coating fracture toughness determined by Vickers indentation: an important parameter in cavitation erosion resistance of WC-Co thermally sprayed coatings, Surf. Coat. Technol. 177-178 (2004) 489–496.
[44] K. Niihara, R. Morena, D.P. Hasselman, Evaluation of K_{IC} of Brittle Solids By the Indentation Method With Low Crack To Indent Ratios, J. Mater. Sci. Lett. 1 (1982) 13–16.
[45] L.-M. Berger, D. Schneider, M. Barbosa, R. Puschmann, Laser acoustic surface waves for the non-destructive characterisation of thermally sprayed coatings, Therm. Spray Bull. 5 (2012) 56–64.
[46] G. Bolelli, A. Candeli, L. Lusvarghi, A. Ravaux, K. Cazes, A. Denoirjean, et al., Tribology of NiCrAlY+Al_2O_3 composite coatings by plasma spraying with hybrid feeding of dry powder+suspension, Wear 344-345 (2015) 69–85.
[47] G. Bolelli, L.M. Berger, M. Bonetti, L. Lusvarghi, Comparative study of the dry sliding wear behaviour of HVOF-sprayed WC-$(W,Cr)_2C$-Ni and WC-CoCr hardmetal coatings, Wear 309 (2014) 96–111.
[48] G. Bolelli, Tribology of metallic and hardmetal thermal spray coatings at high temperature, in: Proceedings of the Workshop on Thermal Spray and Laser Clad Coatings - Coatings for High Temperature Applications, Plzeň, Czech Republic, 2014.
[49] E. Bergonzini, G. Bolelli, B. Bonferroni, L. Lusvarghi, T. Varis, U. Kanerva, et al., Wear behaviour of HVOF-sprayed nanostructured WC-CoCr coatings, in: B. R. Marple, A. Agarwal, M.M. Hyland, Y.-C. Lau, C.-J. Li, R.S. Lima, et al., (Eds.), Thermal Spray 2011: Proceedings of the International Thermal Spray Conference - DVS Berichte, Volume 276, DVS Media GmbH, Düsseldorf, Germany, 2011.
[50] I.T. Jolliffe, Principal Component Analysis, second edition, Springer-Verlag, New York, NY, USA, 2002.
[51] L.-M. Berger, Coatings by thermal spray, in: V.K. Sarin, D. Mari, L. Llanes, C. Nebel (Eds.), Comprehensive Hard Materials, Elsevier, Amsterdam, NL, 2014, pp. 471–506.
[52] I. Hussainova, J. Pirso, M. Antonov, K. Juhani, S. Letunovitš, Erosion and abrasion of chromium carbide based cermets produced by different methods, Wear 263 (2007) 905–911.
[53] C.J. Li, G.C. Ji, Y.Y. Wang, K. Sonoya, Dominant effect of carbide rebounding on the carbon loss during high velocity oxy-fuel spraying of Cr_3C_2-NiCr, Thin Solid Films 419 (2002) 137–143.
[54] H. Warlimont, Ceramics, in: W. Martienssen, H. Warlimont (Eds.), Springer Handbook of Condensed Matter and Materials Data, Springer, Berlin, Germany, 2005, pp. 431–476.
[55] W.D. Callister, Materials Science and Engineering: an Introduction, John Wiley & Sons, Inc, New York, NY, USA, 2007.
[56] A. Verstak, V. Baranovski, AC-HVAF sprayed tungsten carbide : properties and applications Proceedings of the 2006 International Thermal Spray Conference, in: B.R. Marple, M.M. Hyland, Y.-C. Lau, R.S. Lima, J. Voyer (Eds.), ASM International, Materials Park, OH, USA, 2006, pp. 643–648.
[57] P. Vuoristo, Thermal spray coating processes, in: S. Hashmi, G. Ferreira Batalha, C.J. Van Tyne, Y. Bekir, D. Cameron (Eds.), Comprehensive Materials Processing - Volume 4: Films and Coatings: Technology and Recent Development, Elsevier, Amsterdam, NL, 2014, pp. 229–276.
[58] M. Venkatraman, J.P. Neumann, The C–Cr (carbon–chromium) system, Bull. Alloy Phase Diagr. 11 (1990) 152–159.
[59] V.N. Eremenko, T.Y. Velikanova, A.A. Bondar, The phase diagram of the Cr–W–C system at high temperatures, Dokl. Akad. Nauk Ukr. SSR, Seriya A, Fiz. Ta Tekhnichni Nauk., 1986, 11, pp.74–78.
[60] S. Matthews, M. Hyland, B. James, Long-term carbide development in high-velocity oxygen fuel/high-velocity air fuel Cr_3C_2-NiCr coatings heat treated at 900 °C, J. Therm. Spray Technol. 13 (2004) 526–536.
[61] D. Cheng, Q. Xu, G. Trapaga, E.J. Lavernia, I. Introduction, a numerical study of high-velocity oxygen fuel thermal spraying process. part I: gas phase dynamics, Metall. Mater. Trans. A, 32, (2001) 1609–1620.
[62] S. Kamnis, S. Gu, T.J. Lu, C. Chen, Computational simulation of thermally sprayed WC-Co powder, Comput. Mater. Sci. 43 (2008) 1172–1182.
[63] J. Nohava, B. Bonferroni, G. Bolelli, L. Lusvarghi, Interesting aspects of indentation and scratch methods for characterization of thermally-sprayed coatings, Surf. Coat. Technol. 205 (2010) 1127–1131.
[64] Š. Houdková, O. Bláhová, F. Zahálka, M. Kašparová, The instrumented indentation study of HVOF-sprayed hardmetal coatings, J. Therm. Spray Technol. 21 (2011) 77–85.
[65] S. Houdková, O. Bláhová, F. Zahálka, Evaluation of mechanical properties of HVOF sprayed coatings by the CSM indentation method, Chem. List. 104 (2010) s318–s321.
[66] B. Yin, G. Liu, H. Zhou, J. Chen, F. Yan, Sliding wear behavior of HVOF-sprayed Cr_3C_2–NiCr/CeO_2 composite coatings at elevated temperature up to 800 °C, Tribol. Lett. 37 (2010) 463–475.
[67] S. Thiele, K. Sempf, L.-M. Berger, J. Spatzier, Thermophysical and microstructural studies on thermally sprayed chromium carbide coatings. in: Thermal Spray 2011: Proceedings of the International Thermal Spray Conference - DVS Berichte, Volume 276, DVS-Verlag GmbH, Düsseldorf, Germany, 2011, pp. 137–142.
[68] Y.C. Tsui, T.W. Clyne, An analytical model for predicting residual stresses in progressively deposited coatings part 1: planar geometry, Thin Solid Films 306 (1997) 23–33.
[69] B.D. Hosterman, J.W. Farley, A.L. Johnson, Spectroscopic study of the vibrational modes of magnesium nickel chromite, $Mg_xNi_{1-x}Cr_2O_4$, J. Phys. Chem. Solids. 74 (2013) 985–990.
[70] F. Tuinstra, L. Koenig, Raman spectrum of graphite, J. Chem. Phys. 53 (1970) 1126–1130.